UNIVERSIDAD MIGUEL HERNÁNDEZ DE ELCHE

ESCUELA POLITÉCNICA SUPERIOR DE ELCHE

GRADO EN INGENIERÍA DE TECNOLOGÍAS DE TELECOMUNICACIÓN

Frequency shifting loops for optical pulse compression

TRABAJO FIN DE GRADO

Julio - 2021

AUTOR Arnau Busqué Nadal

DIRECTORES Carlos Rodríguez Fernández-Pousa
Germán Torregrosa Penalva

UNIVERSIDAD MIGUEL HERNÁNDEZ DE ELCHE

ESCUELA POLITÉCNICA SUPERIOR DE ELCHE

GRADO EN INGENIERÍA DE TECNOLOGÍAS DE TELECOMUNICACIÓN

Frequency shifting loops for optical pulse compression

TRABAJO FIN DE GRADO

Julio - 2021

AUTOR: Arnau Busqué Nadal
DIRECTORES: Carlos Rodríguez Fernández-Pousa
Germán Torregrosa Penalva

Contents

INTRODUCTION 9

1 WORKING PRINCIPLES AND DESIGN 13

2 CHARACTERIZATIONS 17

2.1. High power RF Amplifier 17

2.2. Frequency shifter: AOM 19

2.3. Laser source: ITLA's linewidth 22

2.4. Optical amplifier: EDFA 27

    2.4.1 Gain 28

    2.4.2 Noise 28

2.5. DSO 30

2.6. Interferometer. 32

3 RESULTS 37

3.1. Waveforms 37

3.2. Autocorrelation 43

4 CONCLUSIONS 51

5 APPENDICES 53

A. Talbot effect 53

B. Time-Bandwidth Product 63

C. Self-heterodyne method for linewidth measurement 68
D. Proof of equation 3.3 70

REFERENCES 73

List of Figures

1.1 FSL schematic 14

1.2 Photograph of the FSL 16

2.1 Schematic of the circuit used to characterize the RF amplifier 18

2.2 Characterization of the RF amplifier 19

2.3 Characterization of the AOM 21

2.4 Mach-Zehnder fiber interferometer for delayed self-heterodyne linewidth measurement 22

2.5 Characterization of the laser source: measured line shapes 24

2.6 Characterization of the laser source: linewidth versus optical output power 26

2.7 Characterization of the EDFA: gain 28

2.8 Characterization of the EDFA: noise 31

2.9 Characterization of the DSO 33

2.10 Characterization of the interferometer: collected data 34

2.11 Characterization of the interferometer: results 34

3.1 Intensity traces 38

3.2 Measured Talbot planes 38

3.3 The effect of a high trigger in the DSO 39

3.4 FSL heterodyne waveforms and their FFT spectra 41

3.5 SPWVD and instantaneous frequency of the chirped waveforms 42

3.6 Quadratic phase of the heterodyne signal 42

3.7 Lasing effect 44

3.8 Simulated field's PACF 46
3.9 Autocorrelation 47
3.10 The effect of windowing the PSD 48
3.11 Resolution 49

5.1 Diffraction of a wave on an amplitude grating 55
5.2 Examples of fractional Talbot effect 62
5.3 Schematic of the autocorrelation peak 64
5.4 Schematic of arbitrary periodic waveforms 65

Introduction

Radar (radio detection and ranging) and lidar (light detection and ranging) techniques represent one of the most successful approaches for remote sensing. This type of systems have found widespread use for different applications, from large-scale sensing (e.g. measuring the position of the moon with millimeter precision) to medium-scale (e.g. obstacle detection for autonomous vehicles) or even very small scales such as targeting single molecules. Using electromagnetic waves, either in radio-frequency (RF), microwave (MW), or optical bands, they are able to measure the target's velocity, distance, or absolute position.

Though speed measurements may be performed using continuous waves, distance and position require pulsed sources. Therefore, a variety of techniques have been developed to generate adequate waveforms, for which the general goal is to increase both the pulse's bandwidth and duration as much as possible —improving the resolution and range of the system, respectively. The product of these two parameters is referred to as time-bandwidth product (TBP) or, equivalently, compression ratio, and is a commonly used figure of merit. Pulse compression methods increase the TBP of a probe pulse by means of frequency/phase modulation or coding. In the case of linear frequency modulation of a pulse, the TBP is increased through its bandwidth, in a process that is usually known as *chirping* and which leads to the well-known chirped pulse radar. As for the coding techniques, the goal is to modulate a sequence of otherwise transform-limited pulses by use of suitable amplitude or phase codes with good correlation properties, in a similar scheme to that used in spread-spectrum transmission. Here, and in contrast to pulse chirping, the TBP increases through the duration of the coded pulse sequence, which now constitutes the basic probe waveform in pulse compression radar/lidar schemes. After matched-filter detection, implemented either in an analog or digital manner, high-TBP pulses or pulse sequences reflected from a target are virtually compressed to a short pulse carrying the energy of the initial probe waveforms. The gain provided by correlation detection can be utilized to increase range for the same noise level or to increase signal-to-noise ratio for the same range, providing range measurements with a resolution determined by the probe bandwidth.

In this regard, photonic systems are usually advantageous with respect to their RF/MW counterparts due to the significantly larger available bandwidth (∼THz) [1]. Moreover, the immunity to electromagnetic interference of optical signals, the decreasing cost of optical components, and the versatility provided by fiber or integrated systems make photonic solutions an appealing alternative to conventional, purely electrical, systems. Within this context, a major technical challenge is the development of compact and versatile high-TBP optical waveform generators amenable to integration in optical pulse compression systems.

One of the most recent and promising approaches to high-TBP optical arbitrary waveform generation [2] is enabled by optical frequency combs (OFC) generated by continuous wave (CW) injection-seeded frequency shifting loops (FSL). Briefly, OFC are periodic optical waves whose spectrum is composed of a high number of equispaced and ideally equalized spectral lines. The use of OFC with a high number of spectral lines is particularly suitable for optical pulse compression systems, since the TBP of a periodic waveform equals the number of lines present in its spectrum. In OFC based on FSL, a CW carrier is injected in a fiber loop, where the input wavelength is recursively frequency shifted in one or several sidebands whose spacing is determined by a customized driving tone. An optical amplifier located within the fiber's loop compensates for losses and permits the multiple recirculation of the frequency shifted carrier, resulting in a comb made up of equally-spaced spectral lines. FSL can be implemented by use of an electro-optic modulator (EOM) as a shifting element, leading to a tunable line spacing from hundreds of MHz to tens of GHz. On the other hand, the use of acousto-optic modulators (AOM), although restricted to frequency spacings of some hundreds of MHz, are able to provide a significantly larger number of lines (>100) while avoiding at the same time the use of costly high-frequency electronics [3, 4]. Even smaller line spacing (∼kHz) may be achieved by employing two modulators with opposite frequency shifting [5]. This reduction of the line spacing, which amounts to an increase in the period of the pulse train, represents an advantage in terms of ease of integration with other techniques, such as modulation or sampling, as these also need less stringent electronic requirements.

In addition to the general characteristics of versatility and ease of implementation of FSL, one of the specific advantages of acousto-optic FSL (AO-FSL) in comparison to their electro-optic counterparts is that the shifting element provides a single-frequency up or down-conversion. In other words, each time the CW carrier recirculates within the loop it is shifted by the same amount, so that the n-th frequency in the comb is orginated by the recirculation of the injected carrier n times within the loop. AO-FSL thus generate optical waveforms which show, by construction, a purely single-sided or unilateral optical spectrum. This observation constitutes a simplification in digital pulse compression systems based on coherent receivers and subsequent numerical correlation detection, since the quadrature channel can be easily determined from the in-phase channel by Hilbert transform [2]. A final general advantage of AO-FSL, which will be object of particular attention in the present study, is its ability to generate different temporal waveforms with essentially the same TBP. This feature allows, for instance, the generation of waveforms with low peak-to-average power necessary for high-power optical amplification. Finally, we mention that a natural extension of the AO-FSL basic architecture, namely the generation of two mutually coherent OFC with different spectral spacing necessary for dual-comb spectroscopy (DCS) [6] or all-optical correlation detection [7], can be realized by use of a bidirectional FSL [5].

In our work we explore the unidirectional AO-FSL as a 80-MHz OFC generator for pulse compression systems in the 1.55-μm telecom band. In chapter 1 we expose the general layout and also the devices that comprise the FSL, explaining the generation of the output complex field by use of the theory of temporal Talbot effect [8, 9]. Subsequently, in chapter 2, we show all the characterizations performed for this project (both results and methods). These include our laser's linewidth, the optical amplifier's noise, and the real-time or Digital Storage Oscilloscope (DSO) quantization noise, among others. In chapter 3 we present and analyze our resulting waveforms and provide a comprehensive account of their autocorrelation. In particular, the detection bandwidth is limited by the 6-GHz real-time oscilloscope, so that the observable electrical waveforms are shown to have a TBP of $\sim$65 and a resolution of 2.7 cm. Finally, in chapter 4 we end with our conclusions. Short MATLAB code examples are shown throughout this document, which is concluded with a number of appendices describing (A) the theory of temporal Talbot effect in fiber optics —supported by the spatial Talbot effect—, (B) the definition of TBP and compression ratio as the quotient of the period and the autocorrelation's equivalent bandwidth, (C) the theoretical basis of the self-heterodyne method used for the characterization of our laser's linewidth, and (D) a very simple proof for the allowance of computing the autocorrelation of the real field instead of the complex field (which can be done in real-time) and then Hilbert-transforming.

Chapter 1

Working principles and design

In this chapter we explain how and why FSLs are able to generate chirped optical pulses from a continuous wave injection laser as well as the different designs and configurations that we tested through the development of our project.

While the simplest FSL could be made with only a frequency shifter, it is required to compensate for the losses inside the loop to achieve bandwidths higher than just a few hundreds of MHz. Therefore, aside from the AOFS (Acousto-Optic Frequency Shifter), the loop includes an EDFA (Erbium Doped Fiber Amplifier) and a TBPF (Tunable BandPass Filter) to reduce the ASE (Amplified Spontaneous Emission) noise introduced by this amplifier. Additionally, an isolator and a PC (Polarization Controller) are needed inside the loop to force unidirectional propagation (i.e. negate backscattering) and maintain the polarization, respectively. The schematic of the complete FSL, together with the heterodyne detection is shown in Fig. 1.1, where the order of the components inside the loop represents the implemented system. Notice how the PC is placed right after the amplifying stage[1] since this stage does not maintain polarization.

The goal of the $\nu_0 = 1550$ nm injection-seeded FSL is to generate spectral lines equispaced by $f_s \sim 80$ MHz with minimum losses, where f_s is the tunable frequency shift introduced by the AOFS. Assuming the losses are at least partially compensated by the EDFA, the total bandwidth B and therefore the number of spectral lines N will be limited by the TBPF. This comb-like spectrum implies that the resulting signal is periodic with period $T = \frac{1}{f_s}$. Since the AOFS's frequency shift is either positive or negative but not both (here is positive), these waveforms will have a one-sided spectrum, hence simple detection of the complex envelope by means of heterodyning[2] is possible. As demonstrated in the literature —[10, 9, 1]—, this envelope may be expressed as

$$e(t) = \sum_{n=0}^{N-1} g_n e^{-j\pi f_s \tau_c n(n+1)} e^{j2\pi n f_s t}, \tag{1.1}$$

---

[1] Amplifying stage refers to the combination of the EDFA and the TBPF.

[2] Heterodyne detection allows the preservation of optical phase by referencing the signal with the original LO (Local Oscillator). Only one photodetector (PD) is necessary.

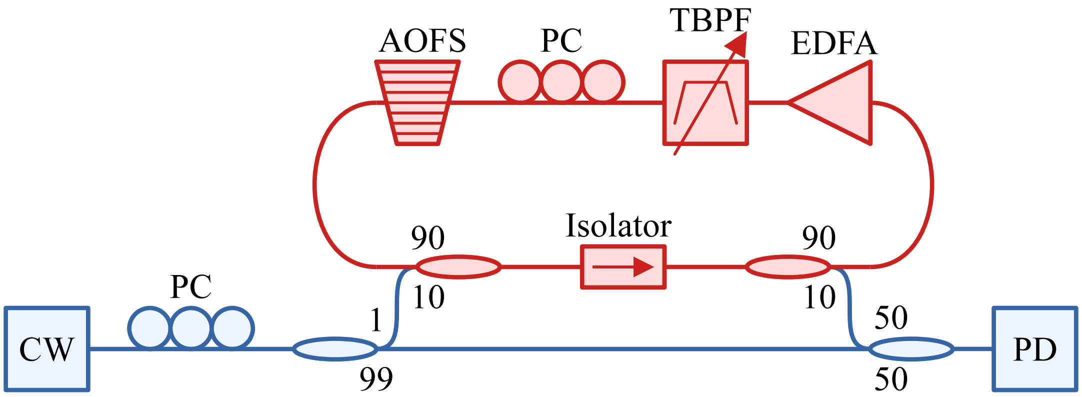

Figure 1.1: FSL schematic. The loop is presented in red, and the heterodyne detection is presented in blue.

where τ_c is the FSL's round-trip time, g_n are the slow exponentially decaying amplitudes of the spectral lines, and a global delay term, $\exp(-j2\pi n\nu_0\tau_c)$, has been neglected in this equation. The quadratic phase of this envelope gives place to the Talbot effect, explained in Appendix A, which means that the period of the FSL's output intensity as well as the chirping effect is completely determined by the product $f_s\tau_c$. With k a positive integer and p and q positive coprime integers:

- If $f_s\tau_c = k$, then the integer Talbot condition is satisfied, resulting in a waveform composed of transform-limited pulses, as all spectral components in Eq. 1.1 are in phase. Both the field $e(t)$ and its intensity have the same period T.
- If $f_s\tau_c = k + \frac{p}{q}$, then the fractional Talbot condition is satisfied. The output field is composed of q transform-limited pulses per period T, leading to pulse repetition-rate multiplication (PRRM) by a factor of q. The period of the intensity is thus T/q. The field, however, maintains the periodicity T, since q consecutive pulses show a set of q different phases which are repeated in the following group of q pulses. This set of phases is usually referred to as the Talbot phase.
- If $f_s\tau_c = k + \frac{p}{q} + \delta f_s\tau_c$, where $|\delta f_s| \ll f_s$ is a slight shift from a Talbot plane, then the previously described pattern undergoes dispersion, and therefore the observed field is composed of chirped pulses. We will refer to this type of situation as the dispersed (fractional or integer) Talbot condition, and characterize it by the associated Talbot index (p/q) and the frequency mismatch (δf_s).

When introducing this δf_s frequency mismatch, the FSL acts as an highly dispersive medium with group delay dispersion (GDD) [1]

$$\phi = \frac{\delta f_s \tau_c}{2\pi {f_s}^2},$$

equivalent, under standard operation conditions, to hundreds or even thousands of standard SMF (Single Mode Fiber) kilometers. In this work we define group velocity dispersion (GVD) as $\beta_2 = \frac{d}{d\omega}\left(\frac{1}{v_g}\right)$, where v_g is the group velocity, and GDD as $L\beta_2 \equiv \phi = \frac{d}{d\omega}\left(\frac{L}{v_g}\right) = \frac{d\tau_g}{d\omega}$. The chirp rate is then given by

$$C = \frac{1}{2\pi\phi}. \tag{1.2}$$

The FSL thus generates a series of waveforms with a repetition rate in the range of 80 MHz, whose temporal profile is determined by the detuning of the AOFS driving frequency f_s. In the pulse compression scenario, the resolution attainable by matched filtering is given by the inverse of the available bandwidth, which in our case is $B = 6$ GHz. The TBP or compression ration is given by the number of spectral lines $N = B/f_s$ of the optical frequency comb, Eq. 1.1. These figures of merits are briefly review in Appendix B.

Although Fig. 1.1 shows the final configuration of the system, some modifications were also tested. The simplest one consists on swapping the 2:1 combiner at the input of the PD for a symmetrical 2 × 2 coupler. This allows the monitoring of the output with an OSA (Optical Spectrum Analyzer). We found this to be useful at the start of the project because it allowed us to see the central wavelength and bandwidth of the TBPF (using the ASE noise). In the end we were able to set the TBPF by looking at the comb spectrum in the DSO without the use of the OSA. We also experimented with a single 2 × 2 symmetrical coupler as a substitute for both the FSL's 90/10 output splitter and the 50/50 combiner at the PD's input. Although the goal of this change is to make the loop shorter —to have a larger number of coherent lines—, the result was significantly less controllable. The last modification that was tested was the use of a 50/50 splitter for the FSL's injection (as a substitute for the 99/1) with the addition of manual variable optical attenuators at its outputs, which permits the control of the FSL's injection power and the heterodyne mix. These attenuators introduced additional degrees of variability that we found to be very useful and were used throughout the majority of the project. However, we discovered that (maybe due to excessive tightening) they modified the polarization of light inside the fiber and, therefore, had to be removed. In Fig. 1.2 we show a photograph of the implemented system.

To conclude this chapter, let us summarize the adjustable parameters of the system. These are: the laser's power, the outer PC, the inner PC, the EDFA's pump current (which affects gain and noise), the TBPF's central wavelength, the TBPF's bandwidth, the AOFS's RF power level, and the AOFS's frequency. The challenge is to adjust all of these parameters to reduce the instability of the resulting waveforms as much as possible while obtaining an appropriate number of spectral lines.

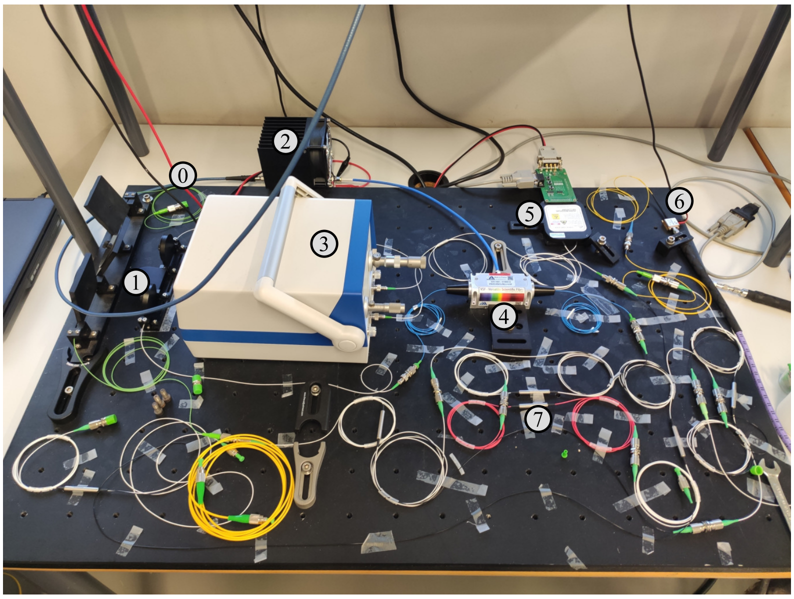

⓪ Injection point

① Polarization controllers

② RF Amplifier

③ Tunable Band-Pass Filter

④ Acousto-Optic Modulator

⑤ Erbium Doped Fiber Amplifier

⑥ Photodiode

⑦ Isolator

Figure 1.2: Photograph of the FSL.

Chapter 2

Characterizations

To properly utilize the physical devices needed for this project and to obtain useful and analyzable empirical results it is of high importance to characterize such devices. In this chapter we show both the experimental and digital processing methods —as well as the results obtained— that were used to characterize the following components: a high-power RF amplifier, an acousto-optic modulator, an ITLA's (Integrable Tunable Laser Assembly) linewidth, and an erbium doped fiber amplifier. Additionally, we also studied the quantization noise of our DSO, and the vibrations and possible noise sources present in the lab that can affect the FSL's interferometer.

2.1 High power RF Amplifier

Device model: Mini-Circuits' *zhl-03-5wf+*.

The purpose of this device together with a signal generator is to feed the RF input of the AOM, which requires around 2 watts of power at 80 MHz. This specific application makes (1) the NF (Noise Figure) somewhat irrelevant —allowing us to focus purely on gain, harmonics, and adaptation— and (2) the process easier and faster since characterization can be done at only one frequency. The manufacturer's datasheet specifies a frequency range from 60 to 300 MHz and 35.31 dB gain at 80 MHz. We must make sure that the amplifier's output power never reaches the power limits that the input port of the SA (Spectrum Analyzer) can withstand. This presents a challenge when trying to determine the 1 dB compression point, $P_{1\mathrm{dB}}$, since this requires high input power that would result in high output power. To solve this issue, we use attenuators and, to reach high input power levels, we use an auxiliary amplifier as shown in Fig. 2.1.

Before the measurement, we ensure that the output power given by our source is stable and correctly displayed in its user interface. For that purpose, a direct measurement of the power source is performed, obtaining a 0.7 dBm deviation from the displayed power which must be considered when analyzing the results. With this procedure, and

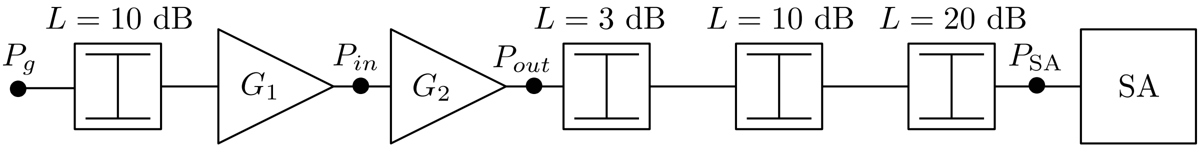

Figure 2.1: Schematic of the circuit used to characterize the RF amplifier. L stands for *attenuation* in dB, G stands for *gain* in dB, P stands for *power* in dBm, and SA stands for *Spectrum Analyzer*. The first amplifier (with gain G_1) is the auxiliary amplifier, while the second one (with gain G_2) is the amplifier under test, that is, Mini-Circuits' *zhl-03-5wf+*. With this scheme, P_g is the signal generator's output power, P_{in} is the input power at the amplifier under test, P_{out} is the output power at the amplifier under test and P_{SA} is the input power at the Spectrum Analyzer. Note that the first attenuator at the amplifier's output must endure high amounts of power.

performing least squares linear regression, we obtain the relationship between output and input power shown in Fig. 2.2a.

Even though P_{1dB} is not reached by our measurements, this is not a problem due to our specific requisite of 33 dBm output power, which we can easily obtain before nonlinearity. Table 2.1 collects the main results found.

Table 2.1: RF amplifier characterization results.

Symbol	Parameter	Conditions	Value	Units
P	Power consumption	$V_{cc} = 24\,\text{V}$ $I = 2.077\,\text{A}$	49.848 (< 67.2)	W
G	Linear zone gain ($average^{\text{i}}$)	@80 MHz $P_{in,max} = 5.12\,\text{dBm}$ ii	34.462 (35.31)	dB
SHD	Second-order Harmonic Distortion iii	@80 MHz $P_{out} = 36.6\,\text{dBm}$	0.996	%
$[S]$	Scattering matrix	@80 MHz	$\begin{bmatrix} -25.14 & -43.61 \\ 34.44 & -21.20 \end{bmatrix}$	dB

In parenthesis: the manufacturer's specification.

i. Gain variance: $\sigma^2 = 0.0021\,\text{dB}$.
ii. No empirical data beyond $P_{in,max}$. This value is still in linear zone as shown in Fig. 2.2a. The manufacturer's datasheet specifies a 1 dB compression point of 5.97 dBm input power.
iii. SHD obtained as a voltage ratio percentage.

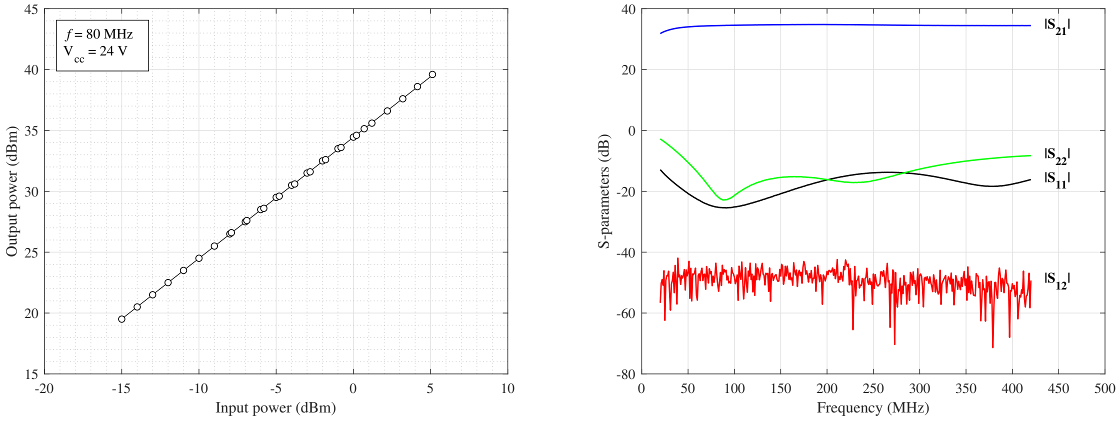

(a) (b)

Figure 2.2: Characterization of the RF amplifier. **(a)** — Output Power vs Input Power. V_{cc} is the DC (Direct Current) supply voltage and f stands for frequency. Collected data is represented with circles and a linear fit is represented with a thin black line. **(b)** — S-parameters. In blue, the transmission coefficient from the input port to the output; in green, the reflection coefficient at the output; in black, the reflection coefficient at the input; and in red, the transmission coefficient from the output port to the input.

The SHD value is increased by the auxiliary amplifier. However, this auxiliary amplifier is working in its linear regime due to the very low power input, which makes the increment negligible. For the measurement of the S parameters, a frequency sweep from 70 MHz to 420 MHz is performed, Fig. 2.2b, with only one 20 dB attenuator and very low input power. Note that two measurements must be done to obtain accurate S_{11} and S_{22} results, one with the attenuator at the amplifier's input and another one with the attenuator at its output. Additionally, due to the 20 dB attenuation, the transmission coefficient from the output port to the input port is below noise level. This is the reason for a noise-like $|S_{12}|$ parameter —despite the already performed correction of 20 dB.

In conclusion, this amplifier is very suited for our needs since it can provide 2 watts of power while still operating in linear zone and the reflection coefficient is especially low at 80 MHz as seen in Fig. 2.2b.

2.2 Frequency shifter: AOM

Device model: AA Opto-Electronic's *MT80-B10-IIR30-Fio-PM0.5-J1-A-VSF*.

In optics, the refractive index of a transparent material can change due to mechanical deformation. Given that sound waves are periodic traveling compression and rarefaction disturbances, an AOM takes advantage of these two phenomena to induce Bragg diffraction on the incident light beam using a piezoelectric transducer. This process results in a sum-frequency generation, that is, if the input optical frequency is ν_{in} and the input radiofrequency is f, the output optical frequency is $\nu_{out} = \nu_{in} + f$. This device, together with the RF amplifier, is necessary for the Frequency Shifting Loop and will also be used to characterize our laser's line shape.

Therefore, characterizing the AOM implies measuring the following relationships:

- RF input reflection coefficient, $|S_{11}|$, versus radiofrequency, Fig. 2.3a.
- Optical power loss versus optical wavelength input, Fig. 2.3b.
- Optical power loss versus radiofrequency input, Fig. 2.3c.
- Optical power loss versus RF power input, Fig. 2.3d.

First, the reflection coefficient is presented, showing its minimum at $\sim$ 78 MHz. For a precise measurement, it is important to use the same type of connectors, otherwise this could generate undesired reflections. For example: although 3.5 mm and SMA connectors are mechanically compatible, the difference in dielectric material will cause an impedance mismatch that could result in an unwanted multiple reflection in the RF path.

Second, optical power loss versus optical wavelength input is presented. While the optimal wavelength seems to be slightly shifted from the manufacturer's specification of 1550 nm to 1542 nm, the device's high bandwidth makes this difference less than 0.1 dB.

Note that the optical power that reaches the AOM must be measured since there will always be losses between the laser source and the optical input port of the device under test. Additionally, an optical polarization controller is used after the laser's isolator.

In both Fig. 2.3a and Fig. 2.3b, a nonlinear least squares fit has been performed. Here we show a MATLAB example:

MatLab Example 1: Nonlinear polynomial fit

```
order = 3; points = 100;
[p,S,mu] = polyfit(x,data,order);
x1 = linspace(min(x),max(x),points);
[fit,delta] = polyval(p,x1,S,mu);
```

Finally, the remaining relationships are presented in figures 2.3c and 2.3d, from which we can see that (1) the optimal input radiofrequency for minimum optical losses is 78

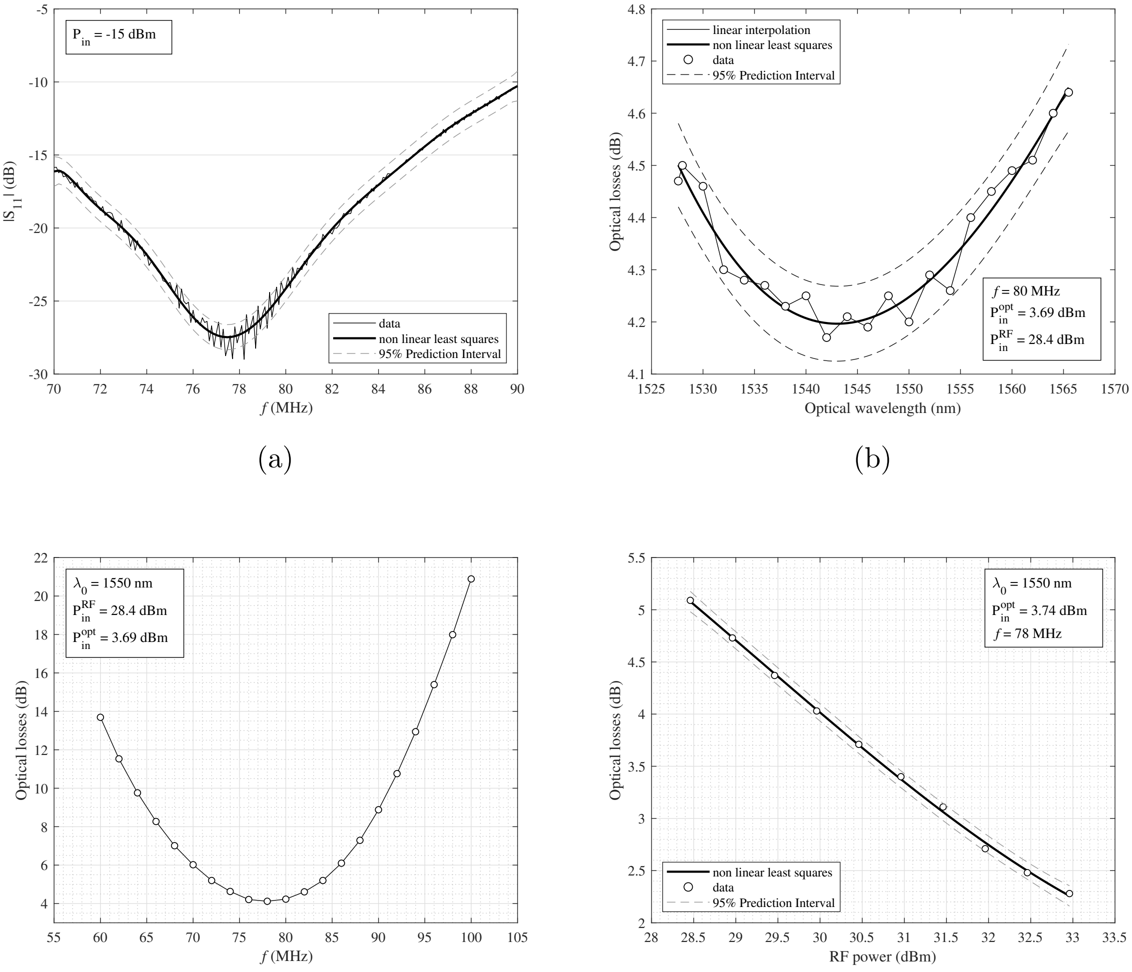

(a) (b)

(c) (d)

Figure 2.3: Characterization of the AOM. **(a)** — RF input reflection coefficient vs radiofrequency. P_{in} is the *input power* and $|S_{11}|$ is the reflection coefficient. **(b)** — optical losses versus optical wavelength. **(c)** — optical losses versus RF. **(d)** — optical losses versus RF power. In all cases, P_{in}^{opt} and P_{in}^{RF} are *optical* and *radiofrequency input power* respectively, f stands for *radiofrequency*, and λ_0 is the *optical wavelength*. Collected data is represented with circles and linear interpolations between data points are represented with thin black lines. Polynomial fits are represented with thick black lines, and their 95% prediction intervals are shown with grey dashed lines.

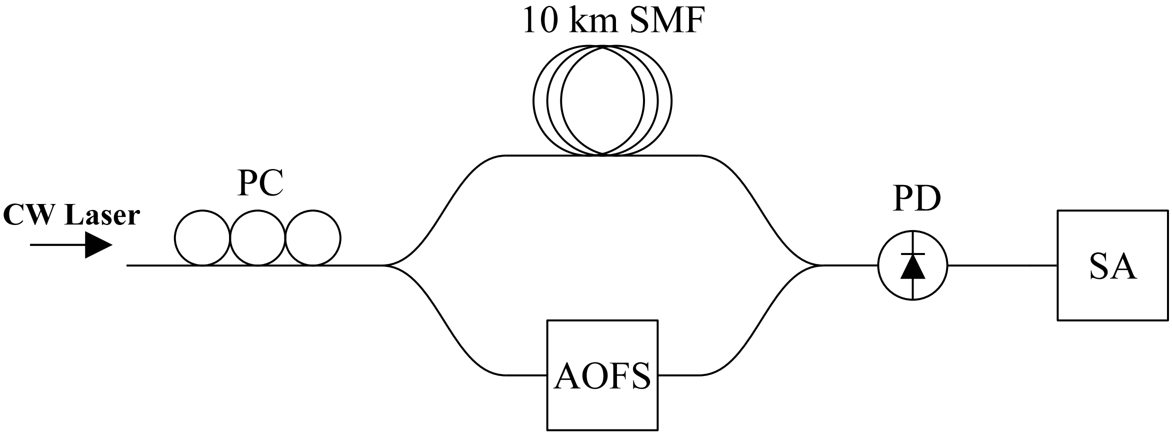

Figure 2.4: Mach-Zehnder fiber interferometer for delayed self-heterodyne linewidth measurement. A continuous wave laser (without dithering) is injected into both arms through a 50/50 splitter (not drawn). The delayed signal and the frequency-shifted signal are then combined with another 50/50 reciprocal splitter (not drawn) and converted by the photodetector. The resulting photocurrent is then analyzed with a spectrum analyzer.

MHz —the nominal value was 80 MHz— and (2) the optical losses as a function of the RF power —to allow for quick, accurate calculations when using the device.

In conclusion, our AOFS has a high optical bandwidth and minimal losses at 78 MHz (which coincides with the best RF adaptation point). Additionally, for RF powers greater than 32.5 dBm at 78 MHz, the optical losses are below 2.5 dB.

2.3 Laser source: ITLA's linewidth

Device model: Keysight Technologies' *N7711A*.

In the FSL, the laser line recirculates up to N times —N being the number of spectral lines— and, therefore, travels a total distance of $N \times L$, where L is the length of the loop. If this distance is greater than the coherence length of the laser, lines corresponding to higher frequencies would lose coherence, which could induce instability. Since the coherence length of the laser is inversely proportional to its linewidth [11, 12], as shown in equations 2.2 and 2.1, a measurement of this width is required to ensure coherence between lines. To measure the laser's spectral linewidth, we use a common method known as delayed self-heterodyne, which in practice consists of a Mach-Zehnder fiber interferometer where one arm has a path length imbalance, and the other arm has a frequency shifter (in this case, an AOM), as show in Fig. 2.4. Analytical explanation of this method can be found in Appendix C.

When performing this experiment there are some factors to account for, apart from the usual problems in fiber optics (dirtiness, bends and, in this case, adjusting the polarization controller). One of them is the possible injection of noise by the 50 Ω resistor in the opto-electric conversion. Since the photocurrent generated by the photodetector will be around 78 MHz, depending on the technology, the resistor may act as an antenna which, in our case, had to be shielded to avoid interference from FM radio channels. However, the most important factor is the design of a suitable fiber length for the delayed arm, which goes hand in hand with the type of laser and its expected line shape. If the laser's linewidth is expected to be around several tens of kHz or more —in our case, a 100 kHz linewidth is expected— an arm length longer than its coherence length should be chosen, resulting in Lorentzian-dominant spectra (f^{-2} noise). In many situations, however, results show a Voigt profile, that is, the convolution of Gaussian and Lorentzian spectra, where none of the two contributions can be discarded. This is, as we present later, what our experimental results show. Then, we can estimate the coherence time of the expected Lorentzian line shape as

$$\tau_{coh} = \frac{1}{\pi \Delta\nu_{\mathrm{FWHM}}} \tag{2.1}$$

and the coherence length as

$$L_{coh} = \frac{c}{n}\tau_{coh}, \tag{2.2}$$

where $n \approx 1.5$ is the refractive index of the optical fiber and c is the speed of light in vacuum. Hence, a 10 km arm length is just enough (one order of magnitude higher than the coherence length) to measure the linewidth of a Lorentzian laser line shape with $\Delta\nu_{\mathrm{FWHM}} \cong 100$ kHz. We must also consider that if the arm is too long, dispersion properties of the fiber play a significant role, resulting in a wider profile. Besides, both arms should, ideally, present the same losses. For a 10 km SMF operating at third window the total attenuation is about 2 dB, which is very similar to losses due to the AOM as shown in Fig. 2.3d.

After designing the arm length, shielding the resistor load, adjusting the polarization (by trying to achieve maximum power output), and making sure there is no dither[1] from the laser source, we can then take measurements for different optical laser powers. Note that each trace may take several minutes to complete due to the need of averaging. Obtained data is shown in Fig. 2.5.

We can see that these profiles resemble Lorentzian profiles which can then be subject to non-linear least squares logarithmic (data is in dBm) Lorentzian fit. In the next lines we describe the processing methods used to obtain the linewidth from our data using MATLAB.

---

[1] Dithering tries to mitigate SBS (Stimulated Brillouin Scattering) by modulating the laser's frequency with a few hundred MHz, which enlarges its linewidth.

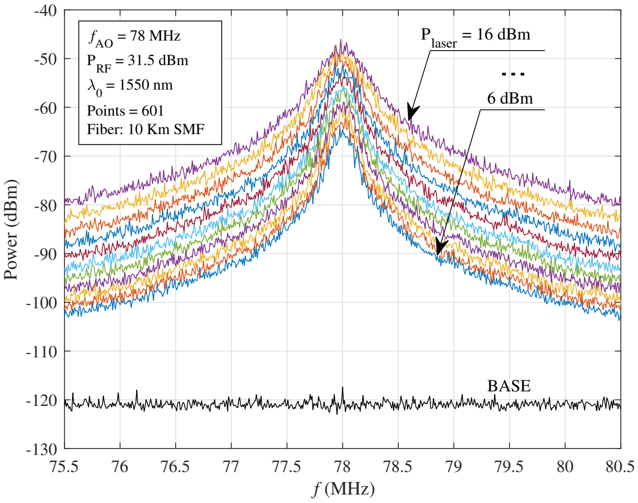

Figure 2.5: Characterization of the laser source: measured line shapes. f_{AO} is the input radiofrequency to the AOM and P_{RF} is its power, λ_0 is the laser's optical wavelength and P_{laser} is its optical power, "Points" is the number of data points of each trace, "Power (dBm)" in the vertical axis refers to the power corresponding to the photocurrent generated by the photodiode to a $50\ \Omega$ resistor, "BASE" trace refers to background noise when the laser is turned off (useful for subsequent digital processing). Traces for different optical laser powers, ranging from 6 dBm to 16 dBm in steps of 1 dB, are presented.

When using numerical methods, it is important to consider every feature of the data that we have previous knowledge of. In this case, for example, the main feature —but not the only one, as we will see— is the fact that our data can be fit with the logarithm of a Lorentzian function:

$$f(x) = 10\log_{10}\left(\frac{a\gamma^2}{\gamma^2 + (x - x_0)^2} + c\right)$$

where 2γ is the FWHM, a is the amplitude of the peak, c is the background additive noise and x_0 is the center frequency, the parameters to optimize. However, we face two problems: (1) our data have magnitudes of about -100 dBm, which in linear form are 10^{-10} mW, and (2) there are several orders of magnitude of difference between parameters. The first problem implies that we would lose numerical resolution when converting to linear, and so the reason we cannot fit the data directly in linear form. The second problem implies that the numerical methods for finding the minimum error may not detect the optimal parameters that we are looking for with our seeds since a slight slope in one direction could be shadowed by a more pronounced one in another. While the first problem is overcome by using $f(x)$, the second problem may be overcome by rearranging the function as

$$\Gamma(f) = -120 + C + 10\log_{10}\left(1 + \frac{A\Delta\nu^2 B}{\Delta\nu^2 + f^2}\right)$$

Now,

- $\gamma \equiv \Delta\nu$,
- $-120 + C = 10\log_{10} c$, the BASE in dB,
- $A = \frac{a}{Bc}$, the quotient between the peak and the base divided by B,
- and $B \cong 10^6$ is a factor that is not meant to be optimized but manually changed instead.

By introducing this factor B, we can compensate the difference in orders of magnitude between a and c. Also, both $\Delta\nu$ and f are in kHz.

All three parameters are now in the same $10^1 \sim 10^2$ order. We can use the `fminsearch` MATLAB function to find the minimum of the squared error. An example code is shown below.

MatLab Example 2: Lorentzian fit

```
B = 1e6; A = 3; delta_v = 30; C = 0;
seed = [A,delta_v,C];

fun = @(x)lorfit(fkHz0,data6dBm,x,B);
x = fminsearch(fun,seed);

y = - 120 + C + 10*log10(1+A*(delta_v^2)*B./(delta_v^2+fkHz0.^2));
y_opt = - 120 + x(3) + 10*log10(1+x(1)*(x(2)^2)*B./(x(2)^2+fkHz0.^2));

function y = lorfit(f, data, x, B)
y = sum((data + 120 - x(3) - 10*log10(1+x(1)*(x(2)^2)*B./...
    (x(2)^2+f.^2))).^2);
end
```

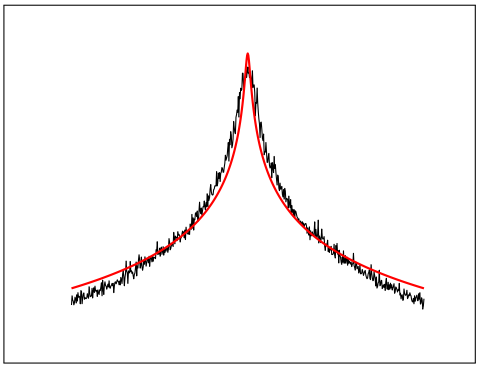

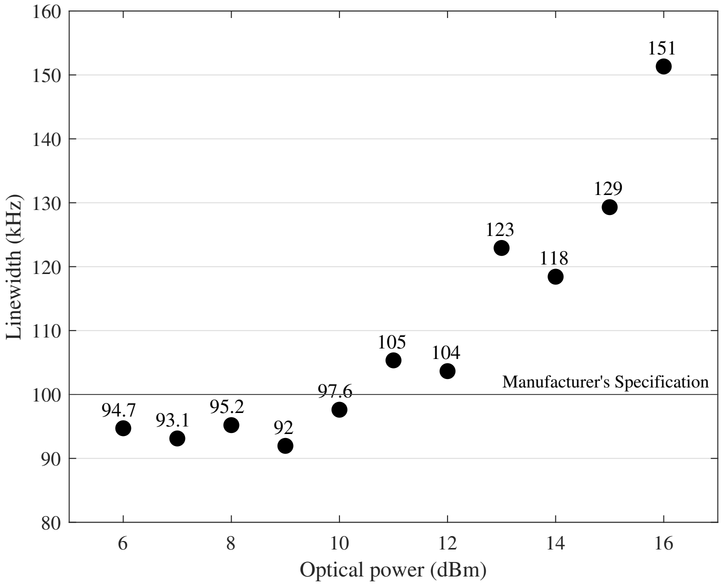

Figure 2.6: Characterization of the laser source: linewidth versus optical output power. Data, represented with black dots, is the FWHM linewidth of our ITLA. The manufacturer's specification for the laser's linewidth is 100 kHz, represented with a black horizontal line. As can be seen, measurements surpass the manufacturer's specification at 11 dBm.

As can be seen in the example above, a Lorentzian fit does not accurately represent our data, which points to the existence of a Gaussian contribution to the linewidth. In this regard, the overall form would thus be a Voigt profile. This, as we hypothesized with a high degree of confidence, is due to the ITLA[2] nature of our laser.

Due to this phenomenon and the unknown characteristics of the Gaussian contribution, Lorentzian nor Gaussian fit would work, while also making a Voigt fit extremely hard. Therefore, we chose to manually measure the linewidth from a polynomial fit. Note that attempting to fit the entire trace would result in a rippled, useless fit, whereby only the vicinities of the peak (at least until the 3 dB fall) are included in the least squares processing. The results are found in Fig. 2.6.

According to Eq. 5.18, the Schawlow-Townes equation, linewidth should decrease with power output as $\Delta\nu \propto {P_{laser}}^{-1}$. However, our ITLA produces an exponential-like increase instead. Linewidth will be less than 100 kHz as long as the laser's optical power output does not exceed 10 dBm.

Also, from the polynomial fit, we may infer that (1) the difference in amplitude of the peaks varies between 1 dB and 2 dB due to polarization fluctuations and (2) the deviation from 78 MHz never surpasses 3 measurement points from the total 601, which, with a resolution of 8.3 kHz, is about 25 kHz.

---

[2] Integrated Tunable Laser Assemblies provide lasing with tunable wavelength and power output. The amplification stages outside the cavity that are used to provide such high optical powers may add additional Gaussian noise.

2.4 Optical amplifier: EDFA

Device model: Orion Laser's *EDFA-EM-B-20-FC/APC*.

To compensate for losses inside the FSL (which are expected to be around 10 dB), an optical amplifier —in this case of Erbium Doped Fiber— must be used. As the name suggests, their working principle is amplification by stimulated emission when pumped with another optical source of different wavelength, typically 980 nm or 1480 nm. The main characteristics of this component are gain and gain saturation, and Noise Figure.

To communicate and issue commands to the device, serial communication software is needed. We used *HyperTerminal*. Furthermore, optical attenuators are necessary to cover a wider range of input powers and to avoid damaging the OSA.

Before starting to take measurements, it is very important to acquire knowledge on how the logical and communication part of the amplifier works, which should be detailed by the manufacturer. In our case:

- Only a communication speed of 115200 bps (bits per second) would work.
- The amplifier has three possible modes of operation: fixed gain, fixed output power, and fixed pump current or "manual mode". The first two modes use variable pump current to always provide the specified gain or specified output power, respectively. The third mode allows to manually specify a fixed pump current, which gives more stability to the output signal.
- The device has a set of alarms that may prevent certain actions. Especially important is the *Loss of Input Signal Alarm*, which completely blocks the amplifier from working properly if the input signal is too low.
- The power output given by the amplifier's internal PD is the total amount of power, including ASE noise. Therefore, not useful when trying to measure the power output at 1550 nm.

The set of attenuators must be previously characterized with a simple optical power meter to make precise measurements.

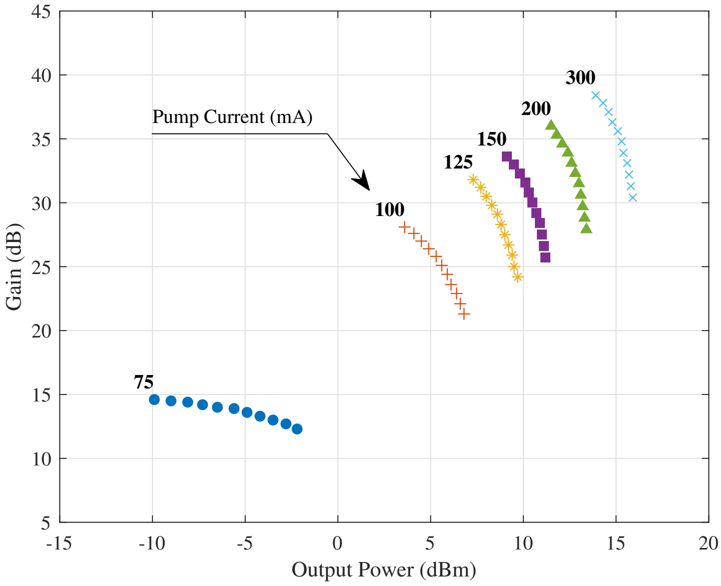

Figure 2.7: Characterization of the EDFA: gain versus output power. The operation mode of the amplifier is "fixed pump current". Several traces are shown, each one for a different pump current value (from 75 mA up to 300 mA). Each trace is represented with a different marker shape and marker color. Note the saturation state of the device for all pump current values and the high gain values.

2.4.1 Gain

The gain of any amplifier is expected to reach a certain saturation point. For optical amplifiers, this point is known as saturation power, P_{sat}, and is defined as the output power that corresponds to a 3 dB decrease of the small signal gain. Utilizing the manual mode of the device we obtain the results shown in Fig. 2.7.

It is evident that the amplifier is already in saturation only at 75 mA and that its gain is extremely high. This is a downside since the purpose of the device is to compensate about 10 dB of losses, which the gain exceeds even with only 75 mA of pump current. Also, as we experimentally tested, the output power is very unstable for pump currents lower than 150 mA, even reaching fluctuations of ± 2 dB at ~ 80 mA. We can infer that the amplifier will operate in saturation regime in the FSL.

2.4.2 Noise

Aside from the amplifier's gain, G, a more significant characteristic is the Noise Figure of the amplifier, which is defined as the ratio between input signal-to-noise ratio ($\mathrm{SNR_{in}}$) and output signal-to-noise ratio ($\mathrm{SNR_{out}}$), i.e. the noise degradation introduced by the device. Let us obtain an expression for NF. By definition,

$$\mathrm{SNR} = \frac{I^2}{\sigma^2},$$

where σ^2 is the noise power and $I = \mathcal{R}P$ is the photocurrent, with P the optical signal's power (P_{in} for the input signal and $P_{\mathrm{out}} = GP_{\mathrm{in}}$ for the output signal), $\mathcal{R} = \eta\frac{e}{h\nu}$ the photodiode's responsivity, e the electron's charge, h the Planck's constant, ν the optical frequency and $\eta \approx 1$ the quantum efficiency. There are four noise contributions [13]—shot noise, σ^2_{shot}; thermal noise, σ^2_t; beat signal-ASE noise, $\sigma^2_{s-\mathrm{ASE}}$; and beat ASE-ASE noise, $\sigma^2_{\mathrm{ASE-ASE}}$. Since thermal noise and beat ASE-ASE noise are negligible for our signal power levels ($P > -25$ dBm), the signal-to-noise ratios are

$$\mathrm{SNR}_{\mathrm{in}} = \frac{(\mathcal{R}P_{\mathrm{in}})^2}{\sigma^2_{\mathrm{shot}}}$$

and

$$\mathrm{SNR}_{\mathrm{out}} = \frac{(G\mathcal{R}P_{\mathrm{in}})^2}{\sigma^2_{\mathrm{shot}} + \sigma^2_{s-\mathrm{ASE}}}.$$

Now, given a certain photodiode's electrical bandwidth, Δf, and the PSD (Power Spectral Density) of ASE in one polarization, S_{ASE}, the noise contributions are $\sigma^2_{\mathrm{shot}} = 2e\mathcal{R}P\Delta f$ and $\sigma^2_{s-\mathrm{ASE}} = 4\mathcal{R}^2GP_{\mathrm{in}}S_{\mathrm{ASE}}\Delta f$. Thus, the signal-to-noise ratios result

$$\mathrm{SNR}_{\mathrm{in}} = \frac{(\mathcal{R}P_{\mathrm{in}})^2}{2e\mathcal{R}P_{\mathrm{in}}\Delta f} = \frac{P_{\mathrm{in}}}{2h\nu\Delta f}$$

and

$$\mathrm{SNR}_{\mathrm{out}} = \frac{(G\mathcal{R}P_{\mathrm{in}})^2}{2e\mathcal{R}GP_{\mathrm{in}}\Delta f + 4\mathcal{R}^2GP_{\mathrm{in}}S_{\mathrm{ASE}}\Delta f} = \frac{GP_{\mathrm{in}}}{(4S_{\mathrm{ASE}} + 2h\nu)\,\Delta f}.$$

Since $S_{\mathrm{ASE}} = n_{sp}h\nu\,(G-1)$, where n_{sp} is the inversion population coefficient (typically, $n_{sp} \approx 1.6$), then the noise figure is

$$\mathrm{NF} = \frac{\mathrm{SNR}_{\mathrm{in}}}{\mathrm{SNR}_{\mathrm{out}}} = \frac{2S_{\mathrm{ASE}}}{Gh\nu} + \frac{1}{G} = 2n_{sp}\left(1 - \frac{1}{G}\right) + \frac{1}{G}.$$

Notice that, for our gains, the additive $1/G$ term —which corresponds to shot noise at the amplifier's output— is negligible. Also, both the amplifier and the ASE noise are removed for $G = 1$, so that $\mathrm{NF} = 1$.

Finally, let us express the noise figure with the OSNR (optical signal-to-noise ratio). This parameter is defined as the margin between the signal power level at the output, GP_{in}, and the ASE noise that is left in the spectral bandwidth $\Delta\nu$ after the output optical filtering done by the EDFA. That is,

$$\mathrm{OSNR} = \frac{GP_{\mathrm{in}}}{P_{\mathrm{ASE}}} = \frac{GP_{\mathrm{in}}}{2S_{\mathrm{ASE}}\Delta\nu}.$$

Provided that the optical filtering is adjusted so that $\Delta f \approx \Delta\nu$, then

$$\mathrm{NF} = \frac{P_{\mathrm{in}}}{\mathrm{OSNR} \cdot h\nu\Delta\nu},$$

which is the final expression that is employed since the OSNR and $\Delta\nu$ are already given by the OSA. Note that the additive $1/G$ term has already been neglected in this expression. Results for OSNR and NF for certain current pump values are presented in figures 2.8a and 2.8b.

As we can see, the noise figure is extremely high for pump currents smaller than 125 mA. However, as the NF decreases, the gain increases, moving away from the desired 10 dB. This behavior induces the need of using high pump currents with attenuators at the output of the amplifier when constructing the FSL. The power levels inside the loop will force the amplifier to operate in saturation.

Because of the specific desire of 10 dB gain, a fixed gain mode test was performed too. Results are presented in Fig. 2.8c. It is clear that the NF is too high to be able to operate the amplifier at such gains unless the input power is greatly increased. Furthermore, this experiment showed that the device was not able to provide the established fixed gain when working with low input power levels.

2.5 DSO

Device model: LeCroy's *SDA6000A*.

To characterize the quantization noise (Q-noise) of our 8-bit 6 GHz DSO, we attempted to analyze the noise floor of single RF tones ranging from 10 MHz to 80 MHz. However, we found that (1) our signal generator was too noisy and (2) a modulation of the RF sine wave with the DSO's sample frequency took place—several peaks separated by an amount equal to the signal's oscillation frequency appeared centered at a sixth and a third of the sample frequency. Additionally, the Q-noise may be correlated to the input signal, especially for low amplitude periodic signals, therefore yielding misleading results. Moreover, we did not manage to acquire full scale traces and instead obtained either very few quantization levels ($\sim$ 10) or many more levels that expected ($\sim$ 3000 to $\sim$ 4000) when using higher voltages. We must clarify that the DSO has an option to increase from 8 to 11 bits, but 2^{11} quantization levels is still lower that the mentioned values. Due to these problems, we used the interferometer's characterization traces —which are explained in the next section— to analyze the Q-noise.

The unilateral power spectral density of the quantization noise may be computed as

$$S_q = 2T_s{\sigma_q}^2, \tag{2.3}$$

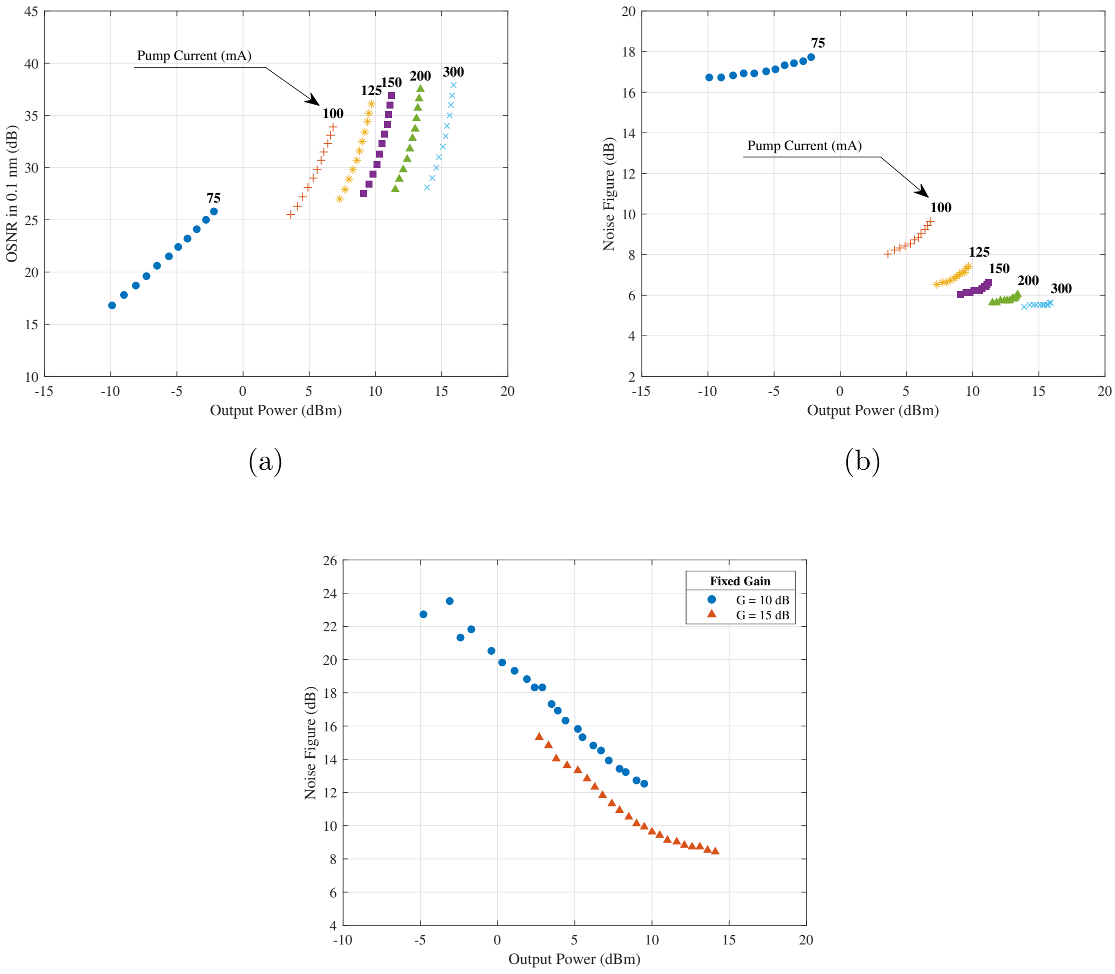

(a)

(b)

(c)

Figure 2.8: Characterization of the EDFA: noise. **(a)** — OSNR versus output power. The OSNR improves as the pump current increases. The value 0.1 nm refers to the optical bandwidth, $\Delta\nu$. **(b)** — Noise Figure versus output power. Note the significant decrease of the NF as the pump current increases. In both figures, the operation mode of the amplifier is “fixed pump current”. Several traces are shown, each one for a different pump current value (from 75 mA up to 300 mA). Each trace is represented with a different marker shape and marker color. **(c)** — NF versus output power for fixed gains of 10 and 15 dB. Data for a fixed gain of 10 dB is represented with blue circles while data for a fixed gain of 15 dB is represented with red triangles. The instability is evident for low powers, and the NF for these gains is high compared to the usual expected values of 4 to 8 dB. The actual gains did not reach the fixed values of 10 and 15 dB.

where T_s is the sampling period and ${\sigma_q}^2 = \frac{q^2}{12}$ is the quantization noise power, with q the quantum in volts. In Fig. 2.9b we see that for a particular trace with sample frequency 10 kS/s, total elapsed time of 100 seconds, and maximum voltage of around 20 mV, the quantum is $q = 0.4419$ mV. This is a common value that we found in many traces. With Eq. 2.3, the Q-noise results $S_q = 3.25 \times 10^{-12}$ V^2/Hz, or in dB: $S_q = -114.87$ dBV/Hz. As we can see in figures 2.9a and 2.9c, this value matches the experimental value. This computation was performed for different traces, always resulting in less than 1 dB discrepancy between the theoretical and experimental values.

Finally, the Q-noise turns out to follow an exponential distribution,

$$f(x) = \begin{cases} \frac{1}{\mu} e^{-\frac{x}{\mu}}, & x \geq 0 \\ 0, & x < 0 \end{cases} \tag{2.4}$$

where μ is the mean. This is shown in figures 2.9c and 2.9d.

2.6 Interferometer

Part of the instability that we found in the output waveforms of the system was due to the mixing stage—the heterodyne detection. Interferometers are highly sensitive to noise and vibrations which, since we did not use an anti-vibrations optical table, became even more significant.

To characterize the interferometer, a simple homodyne system was built. This consists of only the transmitter, a 50/50 splitter, a 50/50 combiner and the receiver. With this setup, several slow acquisition long traces where taken with the DSO, see Fig. 2.10a. The devices with fans or potential vibration/noise sources that were present in the lab are: the RF generator, the RF amplifier, the PD's supply, the laser, two laptops, the DSO, and a loud chiller. Each of the traces mentioned was the result of a certain ON/OFF combination of all of these devices. Additionally, audio recordings of each device were collected to compare their spectral components with the frequency peaks found in these traces.

The final result is shown in Fig. 2.11, where we may highlight four specific frequency components. First, we associated 11.5 Hz to human walking in the building —[14]— as this frequency component has a higher bandwidth. Second, we found that the always-present 100 Hz frequency component was due to the rectified 50 Hz electric signal. Finally, the 90 Hz and 150 Hz are originated by the ILS (Instrument Landing System) of a nearby airport since the location of our lab is almost aligned ($\sim 12°$) with its runway. Also, note the low frequency f^{-2} noise that characterizes the interferometer's stability, which is due to thermal fluctuations.

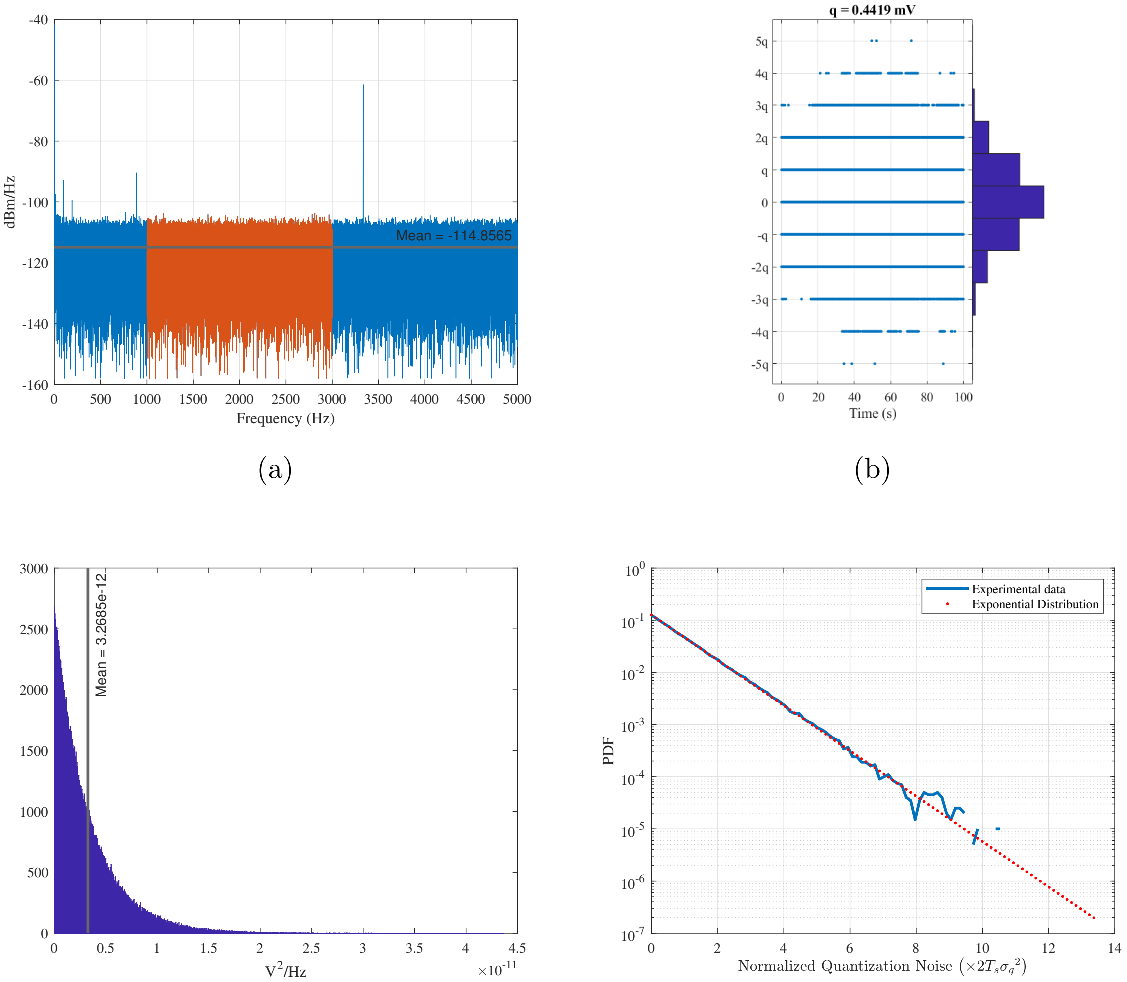

(a) (b)

(c) (d)

Figure 2.9: Characterization of the DSO. **(a)** — Spectral density of the blue trace in Fig. 2.10a, i.e. sample frequency of 10 kS/s and total duration of 100 seconds. In red, the noise-only part of the spectrum used to compute the quantization noise. The mean (in dB) shown in the figure is computed with the linear values and then converted to decibels. Only the values inside the red zone are used. **(b)** — The amplitude difference between consecutive points of the time domain trace and its histogram. q is the quantum. **(c)** — Histogram of 1000 bins computed with the linear values. **(d)** — Probability Density Function (PDF) of the quantization noise, computed with an histogram of 100 bins, in blue. In red dots, an exponential distribution computed with Eq. 2.4 and then normalized so that $\int f(x)dx = 1$. The horizontal axis of the figure is normalized by the mean.

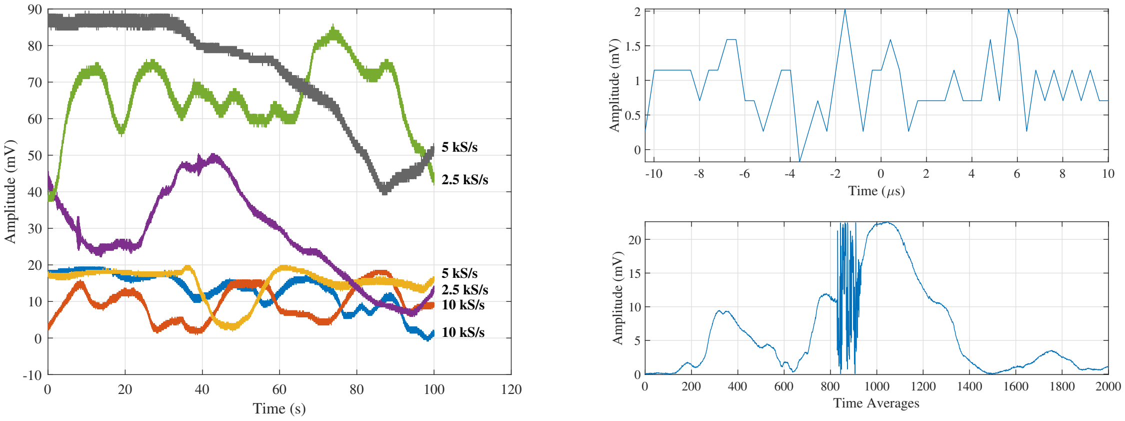

(a) (b)

Figure 2.10: Characterization of the interferometer: collected data. **(a)** — time domain traces. Sample frequency (in samples per second) for each trace is shown in the figure. **(b), top** — a 20 microseconds trace at 2.5 MS/s. **(b), bottom** — time tracing of the average voltage. There are a total of 2000 averages (each of 20 μs) at 20 avg/s (total length of 100 seconds). The interferometer was built with a 50/50 splitter and a 50/50 combiner. A vibration was induced to the interferometer's fiber to show the full scale.

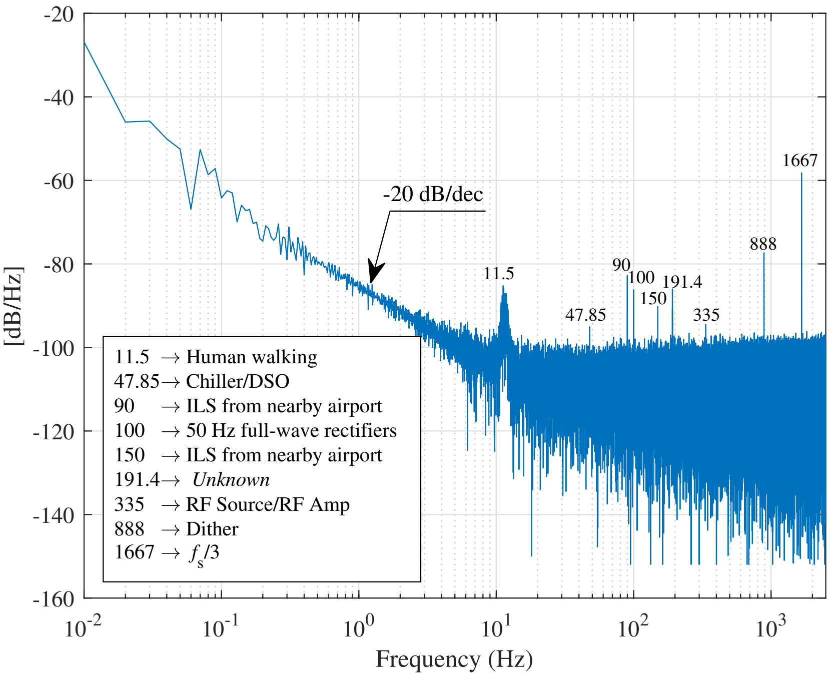

Figure 2.11: Characterization of the interferometer: results. This spectrum corresponds to the grey trace (sample frequency $f_s = 5$ kS/s) in Fig. 2.10a.

To conclude, some time average traces were collected. One of them is presented in Fig. 2.10b, where a vibration on the interferometer's fiber was introduced to see the full scale (~ 22 mV).

Chapter 3

Results

In this chapter we present all the results obtained that characterize the FSL —waveforms, Talbot planes, loop delay, chirp rates, correlation, etc.— and the digital processing methods used as well as some challenges faced when attempting to acquire the data. In all figures, when talking about *injection power* we refer to the output power of the laser, so that its linewidth can be directly retrieved from Fig. 2.6. The optical power feeding the FSL is then 30 dB lower, see Fig. 1.1 for reference.

3.1 Waveforms

First, we characterize the Talbot planes by disconnecting the heterodyne detection, which results in intensity traces like the ones shown in Fig. 3.1. For the measurement of exact Talbot planes, this method is much more effective than heterodyning owing to the visual clarity of the spectral lines—amplitude, spacing, and number of lines. The final result is presented in Fig. 3.2, where a linear fit has been applied to the experimental data obtaining the FSL's round-trip time, $\tau_c = 183.034$ ns (5.46 MHz), and the Talbot integer for $p/q = 0$, $k = 14$. Notice the extremely good coefficient of determination $R^2 = 0.9999992$. Unfortunately, the round-trip time —which is equivalent to a length of $L_c = 36.6$ m— is quite high and, consequently, the coherence decay between lines starts to be significant at 17 lines for a Lorentzian lineshape, Eq. 2.1, and 36 lines for a Gaussian lineshape, $\tau_{coh} = \frac{1}{\Delta\nu_{\mathrm{FWHM}}}\sqrt{\frac{2\ln 2}{\pi}}$ [15]. Due to the frequency-to-time mapping, this loss of coherence produces noticeable instability in the dispersed pulses' tails, as will be explained below.

Before presenting the resulting waveforms, a note on the DSO's trigger must be discussed. We observed that setting a high trigger would greatly —and artificially— increase the chirp rate at lower frequencies as the amplitude of the initial pulse would be considerably higher. In fact, the bandwidth of this high chirp rate zone would be very similar to the bandwidth of this initial pulse. This phenomenon can be seen in Fig. 3.3.

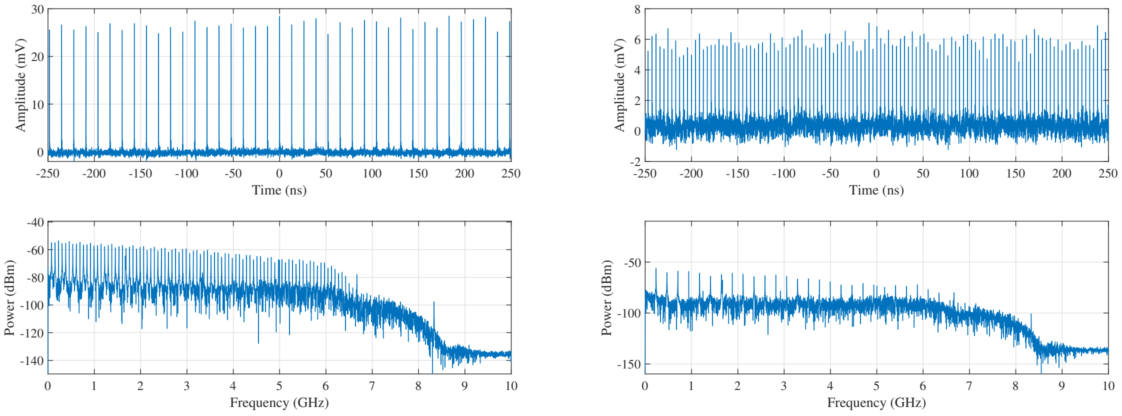

(a) (b)

Figure 3.1: Intensity traces. **(a)** — Talbot plane 0: 76.504 MHz. **(b)** — Talbot plane $1/3$: 78.327 MHz. In both cases, EDFA's pump current is 150 mA (fixed), AOFS's RF level is -1 dBm, injection power is 8 dBm and sample frequency is 20 GS/s. Peak at $6.66 = 20/3$ GHz is due to the DSO's internal clock. Notice the PRRM by a factor of 3.

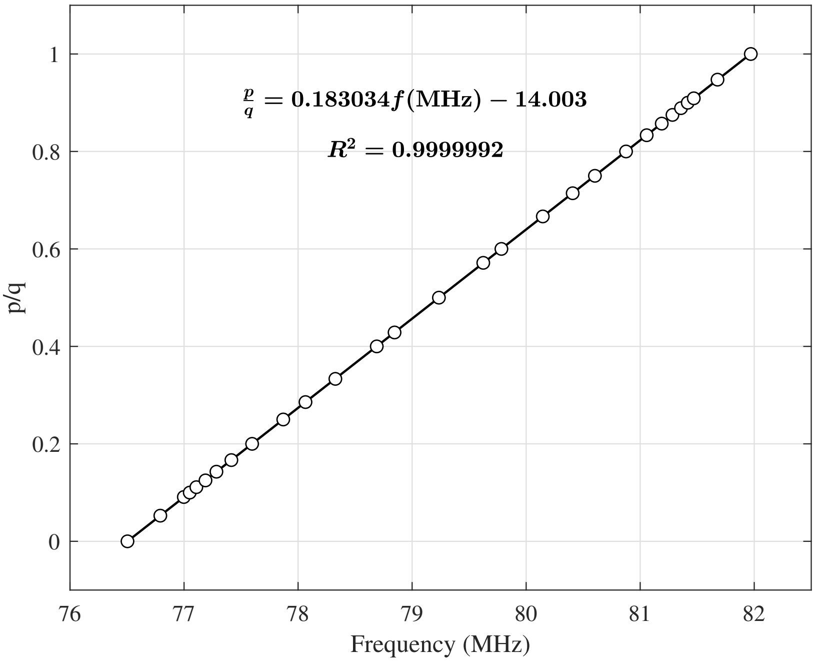

Figure 3.2: Measured Talbot planes. The FSL's round-trip delay results $\tau_c = 183.034$ ns, the Talbot integer for $p/q = 0$ is $k = 14$ and the coefficient of determination is $R^2 = 0.9999992$, computed as $R^2 = 1 - \frac{\sum_i (y_i - f_i)^2}{\sum_i (y_i - \bar{y})^2}$, where y_i are the experimental p/q values, f_i are the fitted values, and $\bar{y}$ is the mean of the experimental values. The smallest measured p/q value is $1/19$ and the biggest (fractional) is $18/19$.

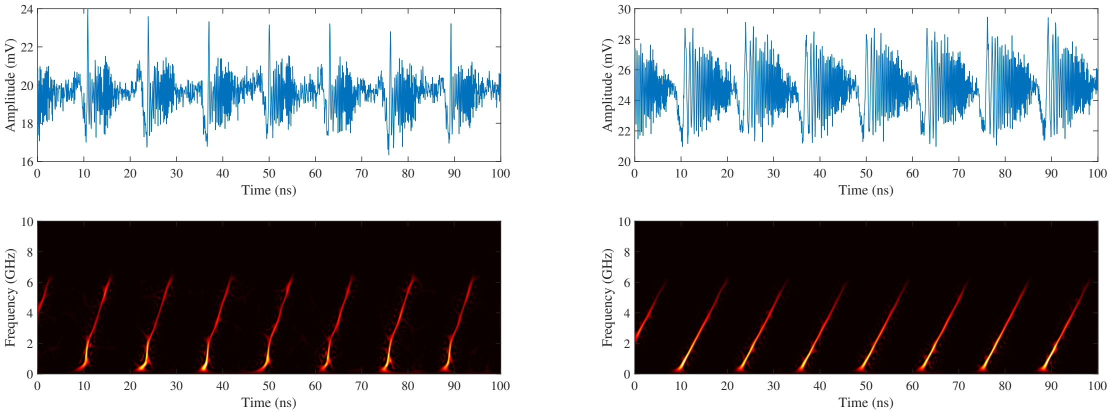

(a) (b)

Figure 3.3: The effect of a high trigger in the DSO. **(a)** — High trigger. Frequency is 76.537 MHz, EDFA's Pump current is 100 mA (fixed), RF level is -1 dBm. **(b)** — Low trigger. Frequency is 76.560 MHz, EDFA's Pump current is 95 mA (fixed), RF level is -2 dBm. Both figures are a slight shift from Talbot plane 0 (76.504 MHz), the sample frequency is 20 GS/s and the injection laser power is 10 dBm. The top plots show the time domain signals while the bottom plots show the Smoothed Pseudo Wigner-Ville Distribution (SPWVD) with a 0 dB threshold.

Some heterodyne waveforms are presented in Fig. 3.4, where the pulse chirping due to induced dispersion is apparent. In a typical configuration, the induced dispersion ϕ takes a value of $\phi \sim 2.8 \times 10^5$ ps/rad (computed for dispersed Talbot 0). Under such a large dispersion, pulses undergo frequency-to-time mapping, so that the pulse profile follows the optical spectrum. In words, the pulse's amplitude content is a (inverted or non-inverted) replica of the optical spectrum, and so the pulse's peak is determined by the wavelengths closer to the injected carrier whereas his tail is determined by the most distant wavelengths. In this plot we also show the fact that the FFT (Fast Fourier Transform) spectra for all these waveforms are the same. This FFT spectra coincides with the optical spectra, and only differs by the slight change in frequency spacing. The different types of temporal signals are due to the different spectral phases in the field's spectrum. The quadratic nature of the phase, which arises as a consequence of the high dispersion undergone by the optical field, is shown in Fig. 3.6 and the SPWVD (Smoothed Pseudo Wigner-Ville Distribution) of these waveforms are shown in Fig. 3.5a, where we show chirp rates up to ~2 GHz/ns and TBPs up to 68. This time-frequency energy distribution is computed with function `wvd` of MATLAB's Signal Processing Toolbox, which uses the following equation for its computation:

$$\mathrm{SPWD}(t,f) = \int_{-\infty}^{+\infty} g(t)H(f)x\left(t+\frac{\tau}{2}\right)x^*\left(t-\frac{\tau}{2}\right)e^{-j2\pi f\tau}d\tau,$$

where $g(t)$ and $H(f)$ are the time and frequency windows, respectively, and $x(t)$ is the

DC filtered analytic[1] signal. For all computations, both windows are Kaiser windows with shape factor 20. Compared to other time-frequency representations such as the spectrogram (windowed Fourier Transform), the SPWVD enables the best possible resolution in both axis and minimizes the interference terms. Besides the SPWVD, the chirps may also be analyzed with the instantaneous frequency —Fig. 3.5b—. This phase jumps represent the capture of the pulse tails' phase by the following pulse [9]. The following MATLAB code shows this computation.

MatLab Example 3: Instantaneous frequency

```
analytic_v = hilbert(v-mean(v));
inst_freq = sampfreq/(2*pi)*diff(unwrap(angle(analytic_v)));
```

We now discuss some considerations with regard to the chirp rates. There are three possible ways to compute these, which we may denote as "theoretical 1", "theoretical 2" and "experimental". Both the "theoretical 1" and "theoretical 2" chirp rates are computed as $C = \frac{{f_s}^2}{\delta f_s \tau_c}$, see Eq. 1.2. The difference relies on the computation of δf_s. In the case of the "theoretical 1" chirp rate, the frequency mismatch is obtained as $\delta f_s = f_s - \frac{k+p/q}{\tau_c}$, with k and τ_c obtained with the linear regression performed in Fig. 3.2. Here, one must be careful with the numerical precision of τ_c and, especially, k. Although the ideal value of k is an integer, at least three decimal places should be used to calculate δf_s. The reason for this is the fact that δf_s is in the kilohertz range, while f_s and τ_c are in the megahertz and nanosecond range, respectively. So,

$$\delta f_s \,(\text{kHz}) \times 10^{-3} = f_s \,(\text{MHz}) - \frac{k + p/q}{\tau_c \,(\text{ns})} \times 10^3 .$$

On the other hand, in the case of the "theoretical 2" chirp rate, the frequency mismatch is simply computed as $\delta f_s = f_s - f_T$, where f_T is the frequency shift corresponding to the exact Talbot plane which value is experimentally obtained (Fig. 3.2). Finally, the "experimental" chirp rate is found by linear regression of the time-frequency distribution of the acquired waveforms. Since these chirps are in the $1 \sim 10$ GHz/ns range, very slight changes in the data sets used for the linear fit can yield significant different results. Moreover, a slight change in these results may also yield significant changes in the relative error with respect to the "theoretical 1" and "theoretical 2" methods. Additionally, we found the dispersed fractional Talbot planes with higher q values to have a lower chirping quality (some undulations may be seen in Fig. 3.5a), due to the fact that these waveforms may experience significant inter-pulse interference, as can be seen in Fig. 3.5b. These effects further contribute to the sensitivity of the linear regression model.

---

[1] The analytic signal is a complex signal whith the real part being the original waveform and the imaginary part being its Hilbert transform.

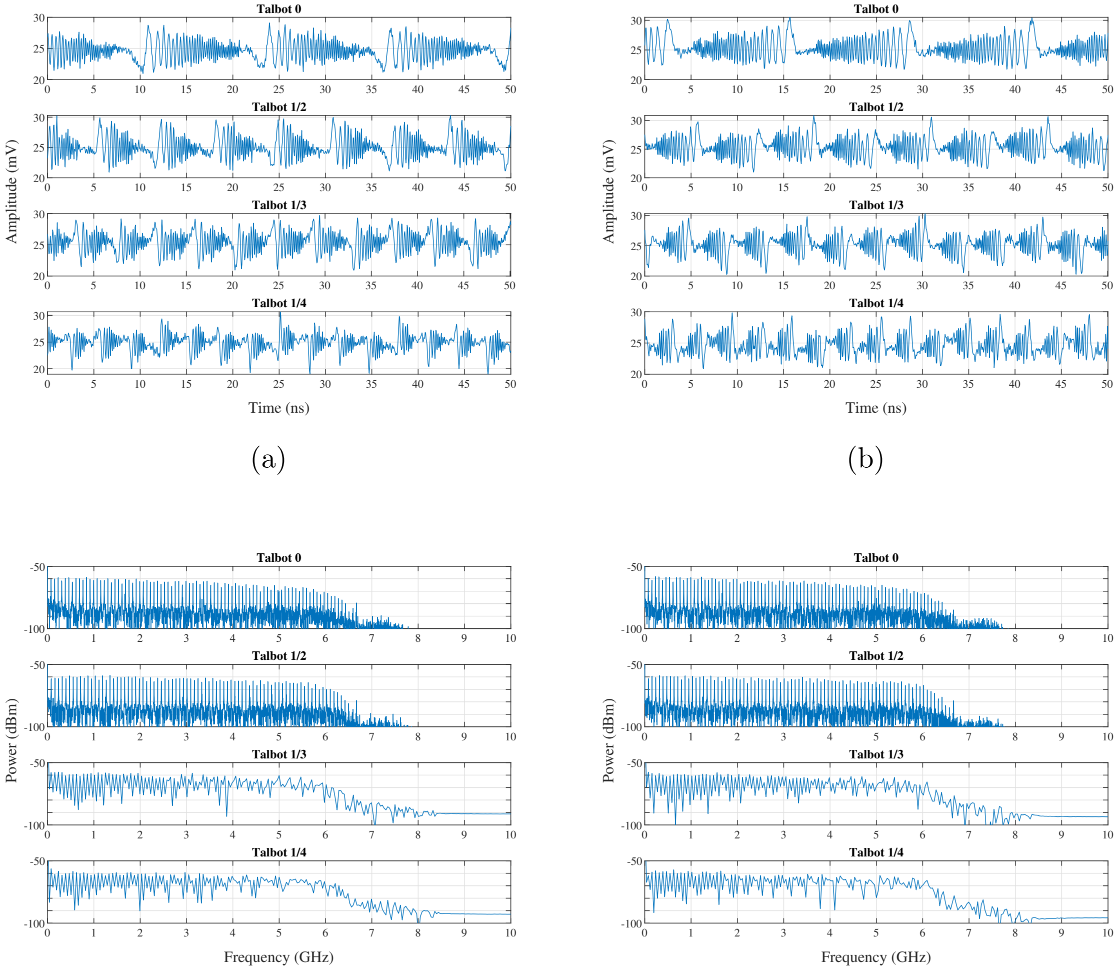

(a) (b)

(c) (d)

Figure 3.4: FSL heterodyne waveforms and their FFT spectra. **(a)** — Positive chirp. From top to bottom, frequencies are 76.560 MHz, 79.260 MHz, 78.344 MHz, and 77.880 MHz. **(b)** — Negative chirp. From top to bottom, frequencies are 76.448 MHz, 79.210 MHz, 78.310 MHz, and 77.860 MHz. Both figures correspond to the dispersion of Talbot planes 0 (76.504 MHz), $1/2$ (79.235 MHz), $1/3$ (78.327 MHz), and $1/4$ (77.870 MHz). Sample frequency is 20 GS/s, injection laser power is 10 dBm, EDFA's pump current is 95 mA (fixed), and RF level is -2 dBm. **(c)** and **(d)** — FFT spectra of waveforms in (a) and (b), respectively. Spectra corresponding to dispersed Talbot planes 0 and $1/2$ are computed from time traces with a total duration of 500 ns (10002 samples) while spectra corresponding to dispersed Talbot planes $1/3$ and $1/4$ are computed from time traces with a total duration of 50 ns (1002 samples).

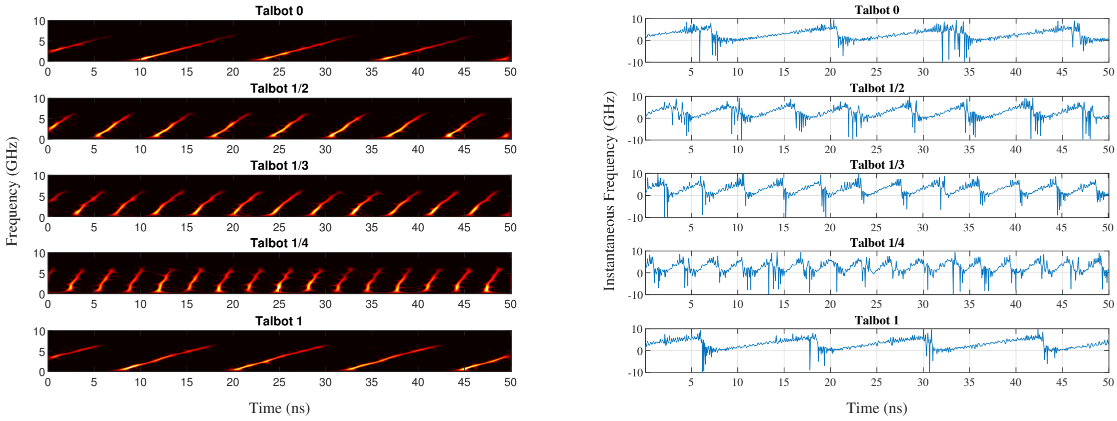

(a) (b)

Figure 3.5: SPWVD and instantaneous frequency of the chirped waveforms. **(a)** — SPWVD of the chirped waveforms. **(b)** — instantaneous frequency. These time-frequency representations correspond to the waveforms presented in Fig. 3.4a plus the dispersed Talbot plane 1 (81.970 MHz) with frequency 82.030 MHz. From top to bottom, the "theoretical 1" chirp rates are 0.570 GHz/ns, 1.404 GHz/ns, 1.763 GHz/ns, 3.213 GHz/ns, and 0.586 GHz/ns; the "experimental" chirp rates are 0.570 GHz/ns, 1.448 GHz/ns, 1.793 GHz/ns, 2.875 GHz/ns, and 0.601 GHz/ns; and the time-bandwidth products are 61, 66, 65, 68, and 68, computed with the autocorrelation's equivalent width, see appendix B.

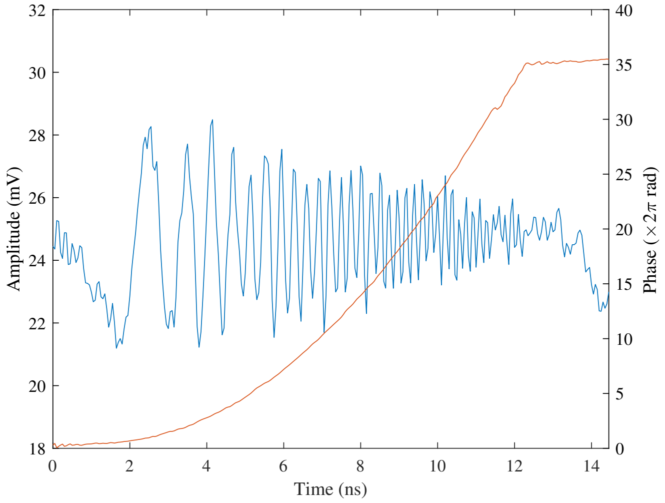

Figure 3.6: Quadratic phase of the heterodyne signal. Frequency is 76.560 MHz, which corresponds to the dispersion of Talbot plane 0 (76.504 MHz). Sample frequency is 20 GS/s, injection laser power is 10 dBm, EDFA's pump current is 95 mA (fixed), and RF level is -2 dBm. The phase capture point is clearly visible at around 12 ns.

The instrumental resolution is 1 kHz, which means that the differential precision (i.e. the error of the frequency mismatch) is $\epsilon_\delta = \sqrt{(1\text{ kHz})^2 + (1\text{ kHz})^2} = \sqrt{2}$ kHz $\approx$ 1.41 kHz. Since dispersed fractional Talbot planes with higher q values require lower frequency mismatches —to reduce the chirp duration and, therefore, minimize inter-pulse interference—, they will present higher relative errors ($\epsilon_{r,\delta} = \frac{\epsilon_\delta}{\delta f_s}$). For instance, $\epsilon_{r,\delta}\left(\delta f_s = 40\text{ kHz}\right) = 3.5$ %, while $\epsilon_{r,\delta}\left(\delta f_s = 10\text{ kHz}\right) = 14.1$ %. Finally, in Table 3.1 we show the relative error between "experimental" and "theoretical 1" chirp rates, ϵ_r, of some waveforms. Here, ϵ_r is computed with $k = 14.002826$ and $\tau_c = 183.034329$ ns. Notice how the error increases with q due to inter-pulse interference.

Table 3.1: Chirp rates.

f_s(MHz)	Exact Talbot plane		Chirp Rate (GHz/ns)		
	freq. (MHz)	p/q	theoretical 1	experimental	ϵ_r (%)
76.560	76.504	0	0.570	0.570	0.01
79.260	79.235	1/2	1.404	1.448	3.05
78.344	78.327	1/3	1.763	1.793	1.69
77.880	77.870	1/4	3.213	2.875	11.77
82.030	81.970	1	0.586	0.601	2.47

Avoiding the lasing effect inside the loop has been a challenge throughout the project due to the high gain of the EDFA. In Fig. 3.7 we show the FSL operating as a mode-locked laser.

3.2 Autocorrelation

Following the nomenclature used in chapter 1, the complex envelope resulting from the FSL is shown in Eq. 1.1. We may write

$$e(t) = \sum_{n=0}^{N-1} e_n e^{j2\pi n f_s t}, \tag{3.1}$$

with $e_n = g_n e^{-j\pi f_s \tau_c n(n+1)}$ the complex amplitude of the n-th harmonic —note that Eq. 3.1 is nothing but an Inverse Discrete Fourier Transform (IDFT). However, the detected signal is $s(t) = \text{Re}\left\{e(t)\right\}$ and, therefore, to obtain the analytic representation, one must compute its Hilbert transform so that $e(t) = s(t) + j\mathcal{H}\{s(t)\}$. Here we denote the real part as $\text{Re}\left\{\cdot\right\}$, the imaginary part as $\text{Im}\left\{\cdot\right\}$, and the Hilbert transform as $\mathcal{H}\{\cdot\}$. The validity of this reconstruction technique is justified by the observation that, from Eq.

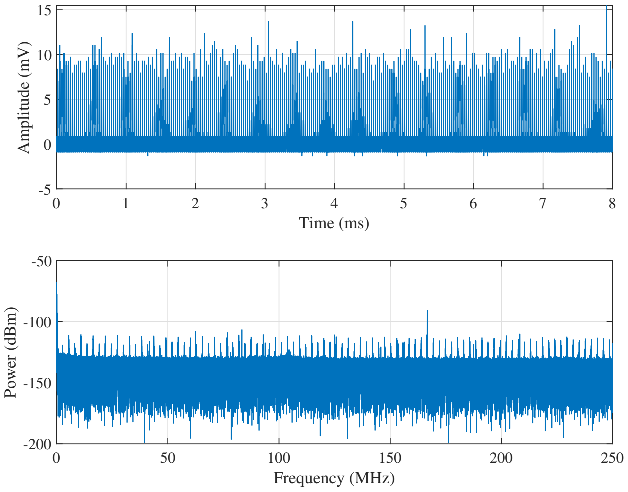

Figure 3.7: Lasing effect. Top plot shows the time domain signal while bottom plot shows the power spectrum. Notice the spectral components multiples of $1/\tau_c = 5.46$ MHz and $1/(2\tau_c) = 2.73$ MHz. The latter are due to aliasing. Injection laser power is 13 dBm (-3 dB from an initial attenuator). Sample frequency is 500 MS/s, EDFA's pump current is 200 mA (fixed), AOFS's frequency is 76.891 MHz, RF level is -1 dBm. Peak at $500/3 = 166.66$ MHz is due to the DSO's internal clock.

3.1, the real part $s(t)$ is composed of a discrete number of cosine functions of different frequency, which under Hilbert transform directly leads to the sine part of the complex exponential. The periodic autocorrelation function (PACF) of the field is, by definition,

$$R_e(\tau) = \langle e^*(t)e(t+\tau)\rangle = \int_0^{1/f_s} e^*(t)e(t+\tau)\,dt, \tag{3.2}$$

where $\langle\cdot\rangle$ is the expected value operator, i.e. the ensemble average. In practice, this computation can only be estimated since just one realization of finite length is available. Using MATLAB's `xcorr` function without any normalization, the estimator is

$$\hat{R}_{xx}(m) = \begin{cases} \sum_{n=0}^{N-m-1} x[n]^* x[n+m], & m \geq 0 \\ \hat{R}^*_{xx}[-m], & m < 0 \end{cases},$$

with N the length of x, which in the case at hand is the complex envelope $e(t)$. However, this estimator is biased. For our purposes, this means that the PACF will present a slow (artificial) decay towards higher lag values. By specifying an *unbiased* flag in this function, the estimator is normalized so that

$$\hat{R}_{xx,unbiased}(m) = \frac{1}{N-|m|}\hat{R}_{xx}(m).$$

This removes the decay, but introduces high variance at higher lag values owing to the low number of data points. The following MATLAB example shows a comparison of these two computations, where a complex field with 10 spectral lines of uniformly distributed random phases has been simulated. To conclude with the bias problem, we mark that a reasonable solution is to use the unbiased estimator and discard the last few periods where the variance is high.

MatLab Example 4: Autocorrelation bias

```
N = 10;
fs = 80e6;
Fs = 20e9;
t = (0:1/Fs:20/fs)';
E = zeros(length(t),1);
phi = rand(N,1)*2*pi;
for i=1:N
    En = exp(1j*(2*pi*i*fs*t + phi(i)));
    E = E + En;
end
R = xcorr(E,E,'biased');
R2 = xcorr(E,E,'unbiased');
```

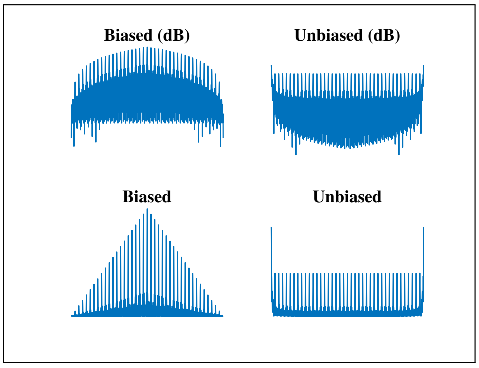

Even though the PACF in Eq. 3.2 is computed with the complex field, it may also be computed with the real signal and then Hilbert-transformed, this is,

$$\frac{1}{2}R_e(\tau) = R_s(\tau) + j\mathcal{H}\{R_s(\tau)\}. \tag{3.3}$$

Proof of this equation is shown in Appendix D. This is an important result, inasmuch as the PACF can be computed in real-time directly with the DSO without loss of the complex envelope. A visual representation is shown in Fig. 3.8a.

Although the PACF can be computed with the estimator (as we have stated), the issues originated by it may be completely solved by developing a model for the PACF, which

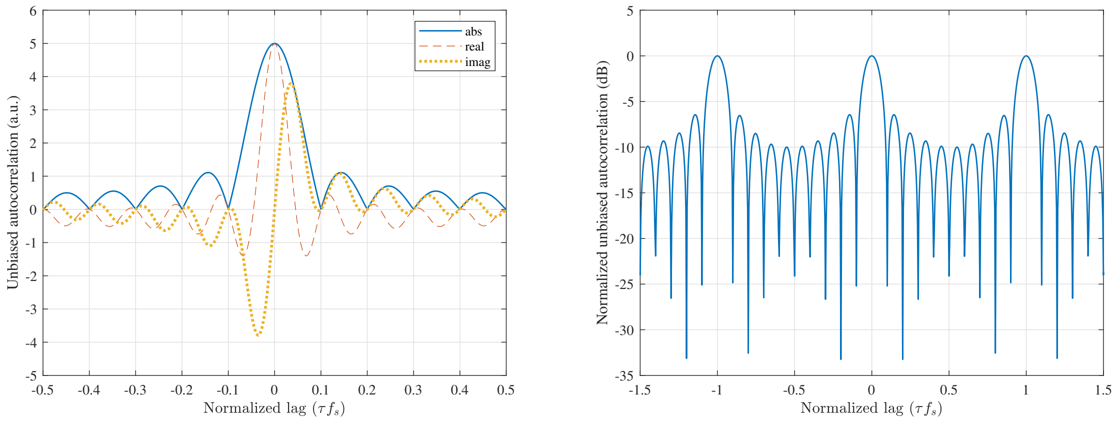

(a) (b)

Figure 3.8: Simulated field's PACF. **(a)** — Comparison of the modulus (blue), real part (red), and imaginary part (yellow) of the PACF. **(b)** — Normalized PACF in dB, $10 \times \log_{10}(|R_e|)$. The peak-to-sidelobe level is 6.53 dB. These figures are the autocorrelation estimation of a simulated complex field with 10 spectral lines of the same amplitude and uniformly distributed random phases. The visual representation of the Hilbert transform in the periodic autocorrelation function is clearly visible, where the imaginary part is phase-shifted by 90 degrees with respect to the real part.

we now present. The model —[10]— is based on the power decay of the spectral lines, $0 < \rho < 1$, so that $|e_n|^2 = P_0\rho^n$, where $P_0 = |e_0|^2$ is the power of the first line of the comb. With a simple computation it is easy to see that

$$R_e(\tau) = \frac{P_0}{f_s}\sum_{n=0}^{N-1}\rho^n e^{j2\pi n f_s t} = \frac{P_0}{f_s}\frac{1-\rho^N e^{j2\pi N f_s \tau}}{1-\rho e^{j2\pi f_s \tau}}. \tag{3.4}$$

We now present our results in Fig. 3.9. As we can see, the model accurately represents the estimation, but it does not predict the sidelobes due to fractional Talbot fields. This is expected, as this model is an approximation for heterodyne detection, [10]. A computation of the PSD from the PACF is shown in Fig. 3.9b to compare the simulation and the experiment. We also attempted to improve the dynamic range of the PACF by windowing the PSD. Although the simulation shows a 10 dB increase, the experiment barely shows any improvement due to the high level of the noise floor. As demonstrated in [9], this noise could be greatly reduced by band-pass filtering each individual spectral line —assuming that a large enough number of temporal periods is available. However, this windowing technique seems to suppress the secondary peaks due to fractional Talbot field 1/2, which is shown in Fig. 3.10. In this digital processing, the power decay ρ^n was corrected before the windowing (equalization). A simple MATLAB example of both processes is shown below, where `R` is the already computed PACF, `Fs` is the sample frequency, and `N` is the number of spectral lines.

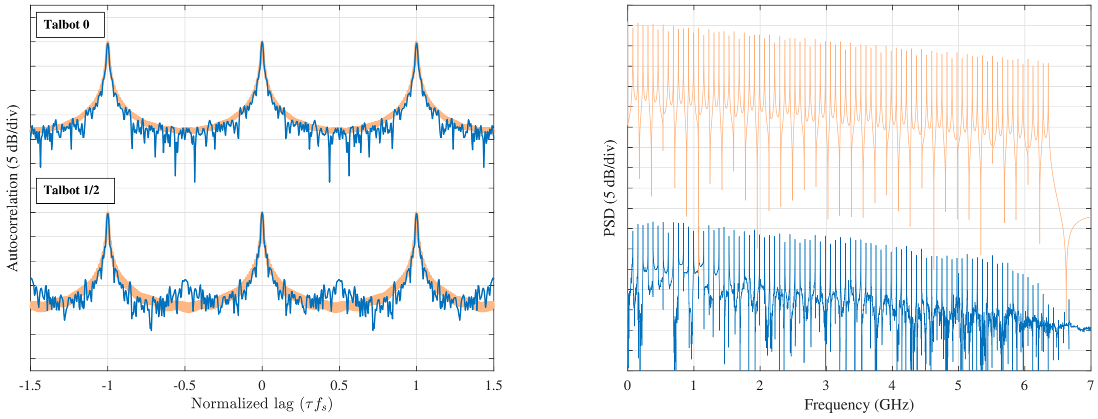

(a) (b)

Figure 3.9: Autocorrelation. **(a)** — Normalized PACF of the experimental heterodyne signal (blue) and simulated PACF (orange) for dispersed Talbot planes 0 and $1/2$. Frequency shifts are $f_s = 76.560$ MHz and $f_s = 79.260$ MHz, respectively. **(b)** — PSD of the experimental heterodyne signal (blue) and simulated PSD (orange) for dispersed Talbot plane 0. Both traces are vertically shifted to improve visual clarity. Sample frequency is 20 GS/s. The simulation parameters are $\rho = 0.9731$ and $N = 84$ for Talbot 0; and $\rho = 0.9818$ and $N = 82$ for Talbot $1/2$. The values for ρ are obtained by fitting the FFT's envelope of the experimental signal. The simulation of the PACF is performed with Eq. 3.4

MatLab Example 5: Equalization of the PSD

```
f = linspace(0,Fs,length(R));
cond = f <= 6e9; cond2 = f > 6e9;
PSD = fft(R);
w = kaiser(length(PSD(cond)),5);
n = 1:N;
decay = rho.^n;
x = linspace(n(1),n(end),length(PSD(cond)));
decay = interp1(n,decay,x);
PSD2 = PSD(cond)./decay';
PSD2 = [PSD2' PSD(cond2)']';
PSD2(cond) = w.*PSD2(cond);
cond3 = find(cond2);
PSD2(cond2) = PSD2(cond3(1)-1);
R2 = ifft(PSD2);
```

To conclude, we end with a table showing the values for (1) the autocorrelation's central peak width, (2) the TBP, and (3) the spatial resolution (Res.) in free space of waveforms

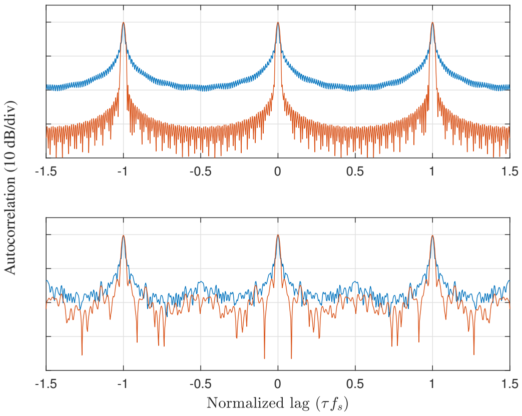

Figure 3.10: The effect of windowing the PSD. In red, the PACF obtained as the inverse FFT of the windowed and equalized PSD for dispersed Talbot $1/2$ ($f_s = 79.260$ MHz). In blue, the original PACF. Top plot shows the simulation —computed with Eq. 3.4, $\rho = 0.9818$ and $N = 82$— and bottom plot shows the experiment. The window used is a Kaiser window with $\beta = 5$ centered at 3 GHz. Notice the significant increase in dynamic range of the simulation, but not on the experiment. However, the secondary peaks are suppressed.

corresponding to dispersed Talbot fields 0, 1/2, 1/3, 1/4, and 1. Two types of widths are computed and compared, which result in slightly different TBPs and resolutions. The effective (Eff.) or equivalent width is computed as shown in Eq. 5.14 in Appendix B while the FWHM width is manually measured from the PACF's width at -3 dB. We can see that, although the FWHM is a good approximation, it gives worse results. The best (ideal) resolution achievable is limited by our 6 GHz DSO, and is $1/(6\,\text{GHz}) = 2.5$ cm. The maximum TBP also follows the same limitation but depends on the frequency shift, f_s, therefore it is shown in the table.

From the values presented, we mention that the best spatial resolution obtained (in free space) is 2.71 cm, for the dispersed Talbot field 1; and the longest range (in free space) is

Table 3.2: TBPs and spatial resolutions in free space.

f_s(MHz)	Exact Talbot		$\Delta\tau$ (ns)		TBP			Res. (cm)	
	freq. (MHz)	p/q	Eff.	FWHM	Eff.	FWHM	Ideal	Eff.	FWHM
76.560	76.504	0	0.215	0.238	60.7	54.8	78.4	3.23	3.58
79.260	79.235	1/2	0.190	0.218	66.3	57.8	75.7	2.85	3.28
78.344	78.327	1/3	0.195	0.210	65.3	60.8	76.6	2.93	3.15
77.880	77.870	1/4	0.190	0.204	67.6	62.9	77.0	2.85	3.06
82.030	81.970	1	0.181	0.198	67.5	61.5	73.1	2.71	2.98

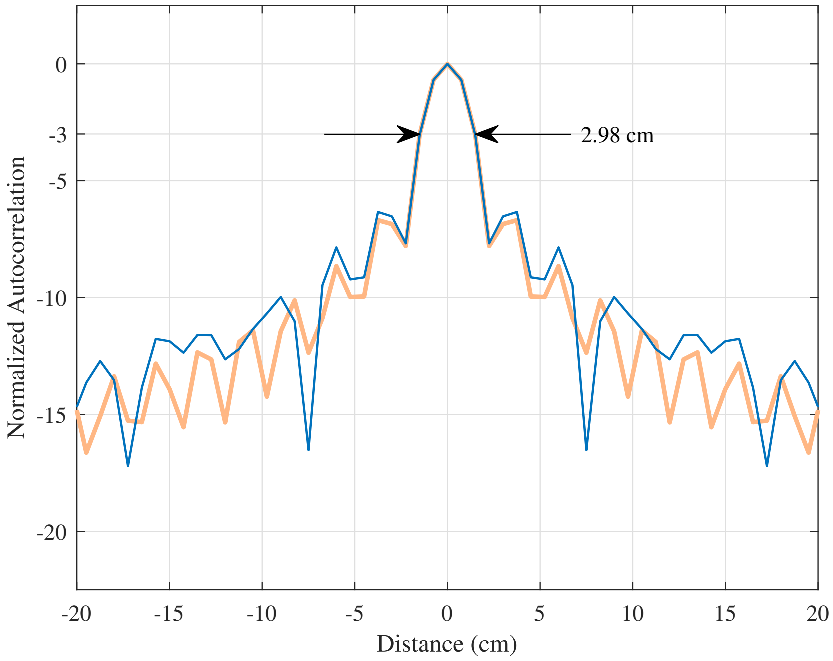

Figure 3.11: Resolution in free space. Zoom into the central peak of the PACF for dispersed Talbot 1 ($f_s = 82.030$ MHz). In blue, the unbiased estimator of the experimental PACF; in orange, the simulated PACF computed with Eq. 3.4 ($\rho = 0.9882$ and $N = 76$).

1.9592 m, for dispersed Talbot field 0 —determined by $1/f_s$. Additionally, in Fig.3.11 we zoom into the PACF's central peak for dispersed Talbot field 1 as an example, illustrating its resolution.

A very simple example for these computations is shown below, where `v` is the real electrical signal, `Fs` is the sample frequency, and `fs` is the frequency shift of the FSL.

MatLab Example 6: TBP, resolution, and range

```
R = xcorr(hilbert(v-mean(v)),hilbert(v-mean(v)),'unbiased');
tau = linspace(-t(end),t(end),length(R))'*fs;
BW = sum(abs(R(tau>=-0.5 & tau<0.5)).^2)/(R(tau==0)^2)/Fs;
TBP = 1/(fs*BW);
resolution = BW*3e8/2;
range = 1/fs*3e8/2;
```

Chapter 4

Conclusions

We have presented an implementation of acousto-optic frequency shifting loops, and studied its use as an optical waveform generator based on an all-fiber optical frequency comb. These systems represent a simple yet versatile, flexible, and cost-effective solution for pulse compression in the optical coherent domain built from a single continuous wave laser. Thanks to the one-sided spectrum of the output field, the approximate complex envelope can be easily retrieved with a single detector by means of heterodyning and Hilbert-transforming —while still allowing for the determination of the exact field with balanced detection.

The resulting comb's spectra, whose line spacings lay around 80 MHz and are determined by the RF signal driving the AOFS, are limited by our digital storage oscilloscope's bandwidth —6 GHz— and present a number of spectral lines close to 80. With pulse durations in the 10 ns scale, optical waveforms having time-bandwidth products in excess of 60 have been demonstrated. In ranging applications, this system is able to provide, after matched-filter detection, resolutions of ~ 2.7 cm in free space in an unambiguous range of 2 m, together with peak-to-sidelobe levels of ~ 15 dB, which cannot be increased through windowing techniques due to the high level of the noise floor. However, windowing the power spectral density has been shown to remove the secondary peaks due to fractional Talbot conditions.

These figures, however, can be improved, as has been demonstrated in the literature. Bandwidths of several tens or even hundreds of GHz can be achieved. This, together with arbitrary line spacings using electro-optic modulators or dual-comb techniques, may result in >1000 lines. Moreover, pulse durations in the μs-scale result in time-bandwidth products that are also in the hundreds. Digital denoising methods have been proven to greatly increase the overall quality of the waveforms and the dynamic range of the autocorrelation. In ranging experiments, these systems would be able to provide millimeter resolution at kilometer distances.

As discussed in the text, some direct and evident improvements can be incorporated to our system. The list includes the incorporation of a low noise (and lower gain) optical amplifier to reduce the total amount of ASE noise within the loop, the increase in detection bandwidth by use of a high-bandwidth DSO, the reduction of coherence issues with a laser source with sub-kHz linewidth, or shortening the total loop length to increase its thermal stability and also improve the coherence of the resulting frequency comb.

In summary, these fiber loops represent an important and useful alternative for optical waveform generation, with demonstrated application in photonic signal processing, including real-time Fourier transformation, electrical waveform generation, spectral estimation, and the particular scenario analyzed here, namely broadband optical waveform generation for its application in optical metrology systems [16, 17] based on pulse compression.

Chapter 5

Appendices

A Talbot effect

The purpose of this appendix is to give understanding of the Talbot effect in fiber optics [8, 18]. Therefore, only the necessary concepts for this goal are explained, focusing merely on their specific application to this phenomenon. To understand the temporal fractional Talbot effect, we first show its spatial integer counterpart.

Fresnel Diffraction

Let us consider the Fresnel diffraction integral as an approximation to the Kirchhoff-Fresnel diffraction for near-field in free space

$$\mathcal{E}(x', y', z) = \frac{1}{j\lambda_0} \iint_{-\infty}^{+\infty} \mathcal{E}(x, y, 0) \frac{e^{jk_0 r}}{r} \frac{z}{r} \, dx \, dy. \tag{5.1}$$

This expression models the diffraction pattern created by waves propagating in z and passing through an aperture, where $\mathcal{E}(x, y, 0)$ is the electric field at the aperture, $k_0 = 2\pi/\lambda_0$ is the wavenumber, $r = \sqrt{(x - x')^2 + (y - y')^2 + z^2}$, and $j = \sqrt{-1}$ is the imaginary unit. We may introduce the Fresnel approximation $(x - x')^2 + (y - y')^2 \ll z^2$, that is, a small aperture compared to the distance z. This allows us to rewrite Eq. 5.1 as

$$\mathcal{E}(x', y', z) = \frac{e^{jk_0 z}}{j\lambda_0 z} \iint_{-\infty}^{+\infty} \mathcal{E}(x, y, 0) e^{\frac{jk_0}{2z}\left[(x-x')^2 + (y-y')^2\right]} \, dx \, dy.$$

For our purpose, we will also assume paraxial propagation so that $(y - y')^2 \approx 0$ and forgo the dependence of z to ease the notation. Thus,

$$\mathcal{E}(x') = \frac{e^{jk_0 z}}{j\lambda_0 z} \int_{-\infty}^{+\infty} \mathcal{E}(x) e^{\frac{jk}{2z}(x-x')^2} \, dx = \frac{e^{jk_0 z}}{j\lambda_0 z} e(x), \tag{5.2}$$

where $e(x)$ is the complex envelope of the spherical wave originated in z, $\frac{e^{jk_0 z}}{j\lambda_0 z}$. For simplicity, we will work with these envelopes instead of the total field.

We can see that Eq. 5.2 represents the propagation of a wave through an aperture as an LTI (Linear Time-Invariant) filter model and may, therefore, be expressed as the convolution of the initial field with the impulse response h of the aperture:

$$e(x') = e(x) * h(x)$$

and

$$h(x) = e^{j\frac{\pi}{\lambda_0 z}x^2}.$$

In the frequency domain, $E'(\nu) = E(\nu)H(\nu)$, where

$$H(\nu) = \mathcal{F}\{h(x)\} = j\lambda_0 z e^{-j\pi\lambda_0 z\nu^2}$$

is the transfer function, $\mathcal{F}\{\cdot\}$ denoting the Fourier Transform. Note that the term $j\lambda_0 z$ will cancel out in the resulting total field, hence we will employ the notation

$$H(\nu) \equiv e^{-j\pi\lambda_0 z\nu^2}.$$

This quadratic dependence of the phase with ν is the key to the Talbot effect.

Spatial integer Talbot effect

Consider the situation shown in Fig. 5.1. This is the case of a periodic amplitude grating that we will assume to be infinite and of spatial period P and alternating amplitude 0 or 1.

The function $t(x)$ describes this spatial structure so that the complex envelope created at the grating is $e(x) = e_0 t(x)$. Due to the periodicity of the grating, $t(x)$ can be expressed as a Fourier series with real coefficients c_k as

$$t(x) = \sum_k c_k e^{j2\pi\frac{k}{P}x}.$$

The Fourier Transform of this function results $T(\nu) = \sum_k c_k \delta(\nu - \frac{k}{P})$, which means that the spectrum of the complex envelope of the electric field at a certain distance z from the aperture plane is given by

$$T'(\nu) = \sum_k c_k \delta(\nu - \frac{k}{P}) e^{-j\pi\lambda_0 z\frac{k^2}{P^2}}.$$

Hence, when the phase difference among consecutive deltas is constant and equal to $n\pi$ (with n integer), whereby they are coherent, the image at z will be an exact copy of the

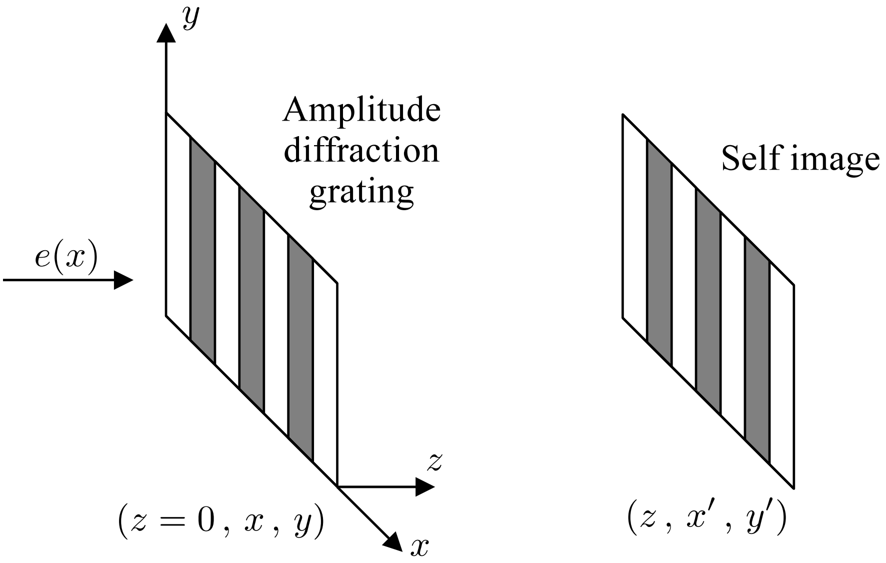

Figure 5.1: Diffraction of a wave on an amplitude grating, resulting in a *self image* at a certain distance.

original structure, known as *self image.* Following this reasoning, we can determine the specific distances for which this phenomenon holds:

$$\Delta\theta \equiv \pi\lambda_0 z\frac{(k+1)^2}{P^2} - \pi\lambda_0 z\frac{k^2}{P^2} = m\pi,$$

$$\pi\lambda_0 z\frac{1}{P^2}(2k+1) = m\pi,$$

$$\lambda_0 z\frac{1}{P^2}l = m, \quad l \in \mathbb{Z}_{odd}.$$

Therefore,

$$\lambda_0 z\frac{1}{P^2} = n$$

and, finally, the *Talbot integer condition*

$$z = n\frac{P^2}{\lambda_0}.$$

In the literature, the basic *Talbot length* is usually defined for $n = 2$ so that the components are in phase,

$$\tilde{z}_T = \frac{2P^2}{\lambda_0}.$$

However, one can also find the condition that includes both even and odd integers, that is, for $n = 1$ so that the components are in antiphase,

$$z_T = \frac{P^2}{\lambda_0}.$$

We shall consider this *shifted* condition in our work.

It must be reinstated that these expressions only hold when $\lambda \ll z$ so that the Fresnel approximation is valid, which is the case when working with optical wavelengths. If the object is periodic but finite, the spectral components of the complex envelope will not be Dirac deltas but rather have a certain width. As long as the phase behaves linearly inside that width, the Talbot effect will be present. As shown in the next section, distances that are rational multiples of these Talbot lengths will also feature copies of the object, but with different period and amplitude.

In conclusion, the basis of the Talbot effect relies on the relationship —integer, fractional, or even fractal— between the phases of each component of a comb —or comb-like— spectrum of some complex periodic structure. This manifests as copies of the original object.

Temporal Talbot effect in fiber optics

Talbot condition and transfer function

Let us consider a modulated optical wave with carrier angular frequency ω_0 and electric field $\mathcal{E}(t) = e(t)e^{j\omega_0 t}$, where $e(t)$ is its periodic complex envelope of period T. This wave propagates inside an optical fiber whose transfer function may be modeled as $H(\omega) = e^{-j\Phi(\omega)} = e^{-j\beta(\omega)L}$. Then, the output field is

$$e'(t) = \frac{1}{2\pi}\int_{-\infty}^{+\infty} E(\omega)H(\omega)e^{j\omega t}d\omega, \tag{5.3}$$

the inverse Fourier Transform of its spectrum $E'(\omega) = E(\omega)H(\omega)$. We may perform a Taylor expansion of $\beta(\omega)$ around the carrier,

$$\beta(\omega) = \beta_0 + \beta_0'(\omega - \omega_0) + \frac{1}{2}\beta_0''(\omega - \omega_0)^2 + \cdots ,$$

where $\beta_0^{(n)}$ denotes $\left.\frac{d^n\beta}{d\omega^n}\right|_{\omega=\omega_0}$. For single mode fiber operating at third window ($\lambda_0 = 1550$ nm), $\beta(\omega)$ can be approximated —with high accuracy— by truncating at the quadratic term, that is, $\beta(\omega) \approx \beta_0 + \beta_0'(\omega - \omega_0) + \frac{1}{2}\beta_0''(\omega - \omega_0)^2$. With this, Eq. 5.3 results

$$e'(t) = \frac{1}{2\pi}e^{j(\omega_0 t - \beta_0 L)}\int_{-\infty}^{+\infty} E(\omega_0 + \eta)e^{j\eta t}e^{-j\beta_0' L\eta}e^{-j\frac{1}{2}\beta_0'' L\eta^2}d\eta,$$

where $\eta = \omega - \omega_0$, the envelope's angular frequency. Note that $\beta_0 L$ is the delay suffered by the carrier and $\beta_0' L$ is the group delay, τ_g, which we assume to be constant. Therefore, with $\tilde{E}(\eta) = \frac{1}{2\pi}E(\omega_0 + \eta)e^{j(\omega_0 t - \beta_0 L)}$ we may write

$$e'(t - \tau_g) = \int_{-\infty}^{+\infty} \tilde{E}(\eta)e^{j\eta t}e^{-j\frac{\beta_0'' L}{2}\eta^2}d\eta. \tag{5.4}$$

Let us recall that the envelope is periodic with period T, hence $\eta \equiv \omega_m = \frac{2\pi m}{T}$. As in the previous section, we may ask ourselves what happens if the quadratic phase term is of the form $n\pi$ or $\frac{p}{q}\pi$, n being integer and p and q being mutually coprime positive integers. Defining $\phi \triangleq \beta_0''L = |\phi|\sigma_\phi$, where σ_ϕ is the sign of ϕ, then

$$e^{-j\frac{\beta_0''L}{2}\eta^2} = e^{-j\phi\frac{\omega_m^2}{2}} = e^{-j|\phi|\sigma_\phi 2\pi^2\frac{m^2}{T^2}} = e^{-j\sigma_\phi\pi\frac{p}{q}m^2} \tag{5.5}$$

and the *Talbot condition* is

$$\boxed{2\pi|\phi| = \frac{p}{q}T^2}. \tag{5.6}$$

Note that this is possible because $e^{j\pi m^2} = (-1)^{m^2} \equiv (-1)^m = e^{j\pi m}$, $m \in \mathbb{Z}$. From Eq. 5.4 and Eq. 5.5 we can see that the transfer function that describes the periodic envelope's propagation is

$$H(\omega_m) = e^{-j\sigma_\phi\pi\frac{p}{q}m^2}. \tag{5.7}$$

To conclude, notice that Eq. 5.6 relates the dispersion in a fiber with the period of the initial train. This, for instance, allows us to compute the specific frequencies that would be needed to satisfy certain fractional Talbot conditions given a total dispersion value, or the necessary fiber length for a given modulation frequency and dispersion coefficient.

Fractional Talbot and Gauss sums

Now, let us express the envelope as the repetition of a certain function $w(t)$ that is contained in a period, $0 \le w(t) < T$:

$$e(t) = \sum_{n=-\infty}^{+\infty} \delta(t - nT) * w(t),$$

where $*$ denotes convolution. We know that, in the spectral domain, $E'(\omega) = E(\omega)H(\omega)$, whereby, using Eq. 5.7, the spectrum of the output envelope results

$$E'(\omega) = \frac{1}{T}\sum_{m=-\infty}^{+\infty} \delta(\omega - \omega_m) e^{-j\sigma_\phi\pi\frac{p}{q}m^2} W(\omega).$$

Therefore, using the Poisson summation formula[1],

$$e'(t) = \sum_{m=-\infty}^{+\infty} e^{-j\sigma_\phi\pi\frac{p}{q}m^2} \delta(t - mT) * w(t) = \frac{1}{T}\sum_{m=-\infty}^{+\infty} e^{-j\sigma_\phi\pi\frac{p}{q}m^2} e^{j2\pi m\frac{t}{T}} * w(t). \tag{5.8}$$

---

[1] $\sum_n f(n) = \sum_k \hat{f}(k)$, where $\hat{f}$ is the Fourier Transform of f.

The goal is to find an equivalent expression to Eq. 5.8 that shows $e'(t)$ as a repetition of $w(t)$ (the final result is shown in Eq. 5.10). For that purpose, we define the repetition function as

$$r(t) = \frac{1}{T} \sum_{m=-\infty}^{+\infty} e^{-j\sigma_\phi \pi \frac{p}{q} m^2} e^{j2\pi m \frac{t}{T}}$$

so that $e'(t) = r(t) * w(t)$.

First we compute the decomposition of the sum by changing the index $m = -\infty, \dots, +\infty$ to $m = nq+l$, where $n = -\infty, \dots, +\infty$ and $l = 0, \dots, q-1$, both integers. It is important to notice that $l = m \pmod q$. With this change, we are arranging $\mathbb{Z}$ into sets of q terms as shown in Eq. 5.9.

$$m = -\infty, \dots, 0, \dots, kq-1, \underbrace{kq, \dots, (k+1)q-1}_{n=k}, (k+1)q, \dots, +\infty \tag{5.9}$$

Infer that the value for l is the same for the i^{th} element in each set. Hence, to perform the sum for all m, we may first sum the i^{th} element for every n (every set) and repeat the process for all l (all the elements in each set):

$$\sum_{m=-\infty}^{+\infty} A_m = \sum_{l=0}^{q-1} \left(\sum_{n=-\infty}^{+\infty} A_{nq+l} \right).$$

Thus,

$$\begin{aligned} r(t) &= \frac{1}{T} \sum_{l=0}^{q-1} \sum_{n=-\infty}^{+\infty} e^{-j\pi\sigma_\phi \frac{p}{q}(nq+l)^2} e^{j2\pi(nq+l)\frac{t}{T}} \\ &= \frac{1}{T} \sum_{l=0}^{q-1} \sum_{n=-\infty}^{+\infty} e^{-j\pi\sigma_\phi \frac{p}{q} l^2} e^{-j\pi\sigma_\phi 2pln} e^{-j\pi\sigma_\phi pqn^2} e^{j2\pi l \frac{t}{T}} e^{j2\pi nq \frac{t}{T}}. \end{aligned}$$

The term $e^{-j\pi\sigma_\phi 2pln}$ is always equal to 1 since it is of the form $e^{-j2\pi k}$ with $k \in \mathbb{Z}$. Additionally, the term $e^{-j\pi\sigma_\phi pqn^2}$ can be simplified as follows:

$$e^{-j\pi\sigma_\phi pqn^2} = (-1)^{\sigma_\phi pqn^2} = (-1)^{\sigma_\phi pqn} = (-1)^{pqn} = (-1)^{e_{pq} n} = e^{-j\pi e_{pq} n},$$

where e_{pq} is the parity of the product pq,

$$e_{pq} = \begin{cases} 0, & pq \text{ even} \\ 1, & pq \text{ odd} \end{cases}.$$

Then, $r(t)$ is:

$$r(t) = \frac{1}{T} \sum_{l=0}^{q-1} e^{-j\pi\sigma_\phi \frac{p}{q} l^2} e^{j2\pi l \frac{t}{T}} \sum_{n=-\infty}^{+\infty} e^{-j\pi e_{pq} n} e^{j2\pi nq \frac{t}{T}}.$$

We can manipulate the summation over n with, again, Poisson formula, noticing that $e^{-j\pi e_{pq}n}$ is just a $\frac{e_{pq}}{2}T$ time shift:

$$\begin{aligned}\frac{1}{T}\sum_{n=-\infty}^{+\infty} e^{-j\pi e_{pq}n}e^{j2\pi nq\frac{t}{T}} &= \frac{1}{q}\sum_{k=-\infty}^{+\infty}\delta(t-\frac{e_{pq}}{2}T-k\frac{T}{q})\\ &= \frac{1}{q}\delta(t-\frac{e_{pq}}{2}T)*\sum_{k=-\infty}^{+\infty}\delta(t-k\frac{T}{q}).\end{aligned}$$

Because $f(x)\delta(x-x_0)=f(x_0)\delta(x-x_0)$, then

$$\begin{aligned}r(t) &= \frac{1}{q}\sum_{l=0}^{q-1}\left[e^{-j\pi\sigma_\phi\frac{p}{q}l^2}\sum_{k=-\infty}^{+\infty}e^{j2\pi l(\frac{e_{pq}}{2}+\frac{k}{q})}\delta(t-\frac{e_{pq}}{2}T-k\frac{T}{q})\right]\\ &= \delta(t-\frac{e_{pq}}{2}T)*\sum_{k=-\infty}^{+\infty}\left[\delta(t-k\frac{T}{q})\frac{1}{q}\sum_{l=0}^{q-1}e^{-j\pi\sigma_\phi\frac{p}{q}l^2}e^{j\pi le_{pq}}e^{j2\pi l\frac{k}{q}}\right],\end{aligned}$$

which means that the complex envelope is

$$\boxed{e'(t)=\delta(t-\frac{e_{pq}}{2}T)*\frac{1}{\sqrt{q}}\sum_{k=-\infty}^{+\infty}e^{j\sigma_\phi\xi_k}\delta(t-k\frac{T}{q})*w(t)} \tag{5.10}$$

where the phases of Eq. 5.10 are given by the following Gauss sums:

$$\begin{aligned}e^{j\sigma_\phi\xi_k} &= \frac{1}{\sqrt{q}}\sum_{l=0}^{q-1}e^{-j\pi\sigma_\phi\frac{p}{q}l^2}e^{j\pi le_{pq}}e^{j2\pi l\frac{k}{q}}\\ &= \frac{1}{\sqrt{q}}\sum_{l=0}^{q-1}e^{-j\pi\sigma_\phi\frac{p}{q}l^2}(-1)^{pql}e^{j2\pi l\frac{k}{q}}\\ &= \frac{1}{\sqrt{q}}\sum_{l=0}^{q-1}e^{-j\pi\sigma_\phi\frac{p}{q}(1+qe_q)l^2}e^{j2\pi\frac{lk}{q}}.\end{aligned} \tag{5.11}$$

In the last part of Eq. 5.11 we have used $(-1)^{pql}=(-1)^{pe_ql^2\sigma_\phi}$. Finally, we can see that the periodic complex envelope at the output is a repetition of $w(t)$ (as the original envelope was) but (1) weighted with $\frac{1}{\sqrt{q}}$, (2) with repetition period $\frac{T}{q}$, (3) shifted $\frac{T}{2}$ if the parity of the product pq is odd, and (4) with phases $e^{j\sigma_\phi\xi_k}$ that follow Gauss sums. The factor $\frac{1}{\sqrt{q}}$ is introduced in these sums so that they are unitary and, therefore, only contribute to the phase. Let us further develop these phases.

With $X_q[l]=e^{-j\pi\sigma_\phi\frac{p}{q}l^2}e^{j\pi le_{pq}}$ and $x_q[k]=\frac{1}{q}\sum_{l=0}^{q-1}X_q[l]e^{j2\pi l\frac{k}{q}}$ we can see that $X_q[l]$ and $x_q[k]$ are a DFT (Discrete Fourier Transform) pair. Let us prove that $X_q[l]$ is q periodic, that is, $X_q[l]=X_q[l+q]$:

Proof. We have that

$$X_q[l+q] = e^{-j\pi\sigma_\phi \frac{p}{q}(l+q)^2} e^{j\pi(l+q)e_{pq}} = e^{-j\pi\sigma_\phi \frac{p}{q}l^2} e^{-j\pi\sigma_\phi 2pl} e^{-j\pi\sigma_\phi pq} e^{j\pi l e_{pq}} e^{j\pi q e_{pq}}.$$

Since, $e^{-j\pi\sigma_\phi 2pl}$ is always equal to 1 and $e^{j\pi q e_{pq}} = e^{j\pi pq^2} = e^{j\pi pq}$, then

$$X_q[l+q] = e^{-j\pi\sigma_\phi \frac{p}{q}l^2} e^{j\pi l e_{pq}} e^{-j\pi\sigma_\phi pq} e^{j\pi pq} = e^{-j\pi\sigma_\phi \frac{p}{q}l^2} e^{j\pi l e_{pq}} e^{j\pi pq(1-\sigma_\phi)}.$$

Now, $e^{j\pi pq(1-\sigma_\phi)}$ is always equal to 1 since the phase is either 0 ($\sigma_\phi = 1$) or a multiple of 2π ($\sigma_\phi = -1$). Hence,

$$X_q[l+q] = e^{-j\pi\sigma_\phi \frac{p}{q}l^2} e^{j\pi l e_{pq}} = X_q[l].$$

□

Let us use **Theorem 1** from [8], this is:

Theorem. *Given two coprime and positive integers, p and q, there exists a unique integer s, verifying*

(a) s lies in the range $1 \leq s \leq 2q-1$,

(b) s is a solution of the congruence:

$$sp = 1 + qe_q \ (mod\ 2q),$$

(c) s has opposite parity to q,

(d) s is coprime with q.

From this theorem, it follows that

$$s = \begin{cases} \left[\frac{1}{p}\right]_{2q}, & q \text{ even} \\ \\ 2\left[\frac{1}{2p}\right]_q, & q \text{ odd} \end{cases},$$

where $\left[\frac{1}{a}\right]_b$ denotes the inverse of a (mod b).

Since s and q are coprime, the set $\{sm \mid m = 0, \ldots, q-1\}$ is a complete set of residues modulus q. Due to the periodicity shown, we may perform the change $l = sm$ in Eq.

5.11 and then $sp = 1 + qe_q$, leading to

$$\begin{aligned} e^{j\sigma_\phi \xi_k} &= \frac{1}{\sqrt{q}} \sum_{m=0}^{q-1} e^{-j\pi\sigma_\phi \frac{p}{q}(1+qe_q)s^2m^2} e^{j2\pi\frac{smk}{q}} \\ &= \frac{1}{\sqrt{q}} \sum_{m=0}^{q-1} e^{-j\pi\sigma_\phi \frac{s}{q}(1+qe_q)^2m^2} e^{j2\pi\frac{smk}{q}} \\ &= \frac{1}{\sqrt{q}} \sum_{m=0}^{q-1} e^{-j\pi\sigma_\phi \frac{s}{q}m^2} e^{j2\pi\frac{smk}{q}} \\ &= \frac{1}{\sqrt{q}} \sum_{m=0}^{q-1} e^{-j\pi\frac{s}{q}(\sigma_\phi m^2 - 2km)}. \end{aligned}$$

Completing to the square of a sum,

$$\boxed{e^{j\sigma_\phi \xi_k} = \frac{1}{\sqrt{q}} e^{j\pi\sigma_\phi \frac{s}{q}k^2} \sum_{m=0}^{q-1} e^{-j\pi\sigma_\phi \frac{s}{q}(m-\sigma_\phi k)^2}},$$

and note that

$$e^{j\sigma_\phi \xi_0} = \frac{1}{\sqrt{q}} \sum_{m=0}^{q-1} e^{-j\pi\sigma_\phi \frac{s}{q}m^2}.$$

Due to the periodicity and symmetry of these Gauss sums and the symmetry property of the DFT, it can be shown that

$$e^{j\sigma_\phi \xi_k} = e^{j\sigma_\phi \xi_0} e^{j\pi\sigma_\phi \frac{s}{q}k^2}.$$

Also, according to the parity of q, $e^{j\sigma_\phi \xi_0}$ can be written as

$$e^{j\sigma_\phi \xi_0} = \begin{cases} \left(\dfrac{s}{q}\right) e^{j\frac{\pi}{4}(q-1)}, & q \text{ odd} \\ \\ \left(\dfrac{q}{s}\right) e^{-j\frac{\pi}{4}s}, & q \text{ even} \end{cases}.$$

where $\left(\frac{a}{b}\right)$ denotes the Jacobi symbol.

Finally, we may conclude that the complex envelope is

$$e'(t) = \frac{1}{\sqrt{q}} \sum_{k=-\infty}^{+\infty} w(t - k\frac{T}{q} - e_{pq}\frac{T}{2}) e^{j\sigma_\phi \xi_k},$$

which means that the new period is T/q and that it is shifted by half a period when both p and q are odd. Therefore, if $w(t)$ (which was contained in a period, T) is nonzero

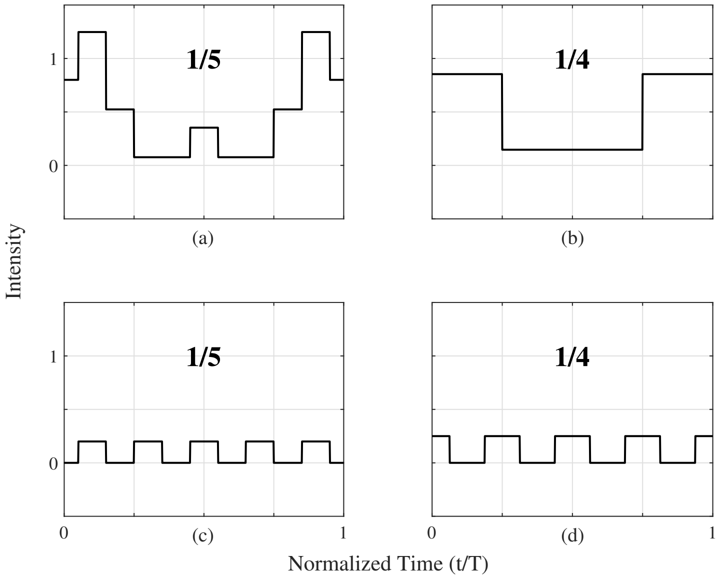

Figure 5.2: Examples of fractional Talbot effect in a unit cell for $p/q = 1/5$ and $p/q = 1/4$. The original pulse duration in (a) and (b) is $T/2$ and, therefore, show overlap, while the duration in (c) and (d) is $T/(2q)$, resulting in a PRRM.

in the range $[T/q, T)$ or $(T/q, T]$, there will be pulse superposition. Some examples for a rectangular pulse are shown in Fig. 5.2a and 5.2b. *Pulse Repetition Rate Multiplication* (PRRM) will then take place when

$$\operatorname{supp}\, w(t) \in \left[0, \frac{T}{q}\right) \quad \text{or} \quad \operatorname{supp}\, w(t) \in \left(0, \frac{T}{q}\right],$$

where

$$\operatorname{supp}\, f(x) = \{x \in \mathbb{R} \mid f(x) \neq 0\}\,.$$

Examples of PRRM are shown in Fig. 5.2c and 5.2d.

B Time-Bandwidth Product

Let us begin with some general results; they can be consulted, for instance, in the book by Levanon and Mozeson [19]. Let us consider a (baseband) pulse $p(t)$, in general complex, such that supp $p(t) \in [0, a]$ for some time scale a. It is assumed an energy-type signal, with energy $E_p = \int_0^a |p(t)|^2 dt$ and Fourier spectrum $P(f)$. The (two-sided) energy spectral density is $S_e(f) = |P(f)|^2$, with f the Fourier frequency. In terms of the spectrum, the energy is $E_p = \int_{-\infty}^{+\infty} S_e(f) df$.

As is well known, the matched filter optimizes its detection in AWGN (Additive White Gaussian Noise) with noise spectral density N_0, so that the output SNR, evaluated a seconds after the entrance of the pulse, is bounded by:

$$\mathrm{SNR}_a \leq \frac{2E_p}{N_0}. \tag{5.12}$$

The bound is attained by the matched filter, $h(t) = p^*(a - t)$. The output $d(u)$ of this filter is given by:

$$d(u) = h(u) * p(u) = \int_{-\infty}^{+\infty} p(t)h(u - t)\, dt = \int_0^a p(t)p^*(t - u + a)\, dt.$$

This output can be expressed in terms of the pulse's autocorrelation, defined as:

$$R_p(u) = \int_{-\infty}^{+\infty} p(t)^* p(t + u)\, dt = R_p(-u)^*$$

so that the output is the autocorrelation delayed by the integration time a,

$$d(u) = R_p(u - a).$$

If the output is sampled after a seconds, it gives the pulse energy, $R_p(0) = d(a) = E_p$. In fact, this is the highest value that the autocorrelation can attain, since $|R_p(u)| \leq R_p(0)$. Also, recall that the autocorrelation is the Fourier transform of the spectrum (Wiener-Kintchine theorem):

$$R_p(u) = \int_{-\infty}^{+\infty} S_e(f)\, e^{j2\pi f u}\, df.$$

In general, one is interested in a situation where $p(t)$ is a radar pulse. Then, one can assume that the instantaneous power $|p(t)|^2$ is a peaked function, which reaches a maximum for some time in the interval $[0, a]$. We define the peak power as $P_{\mathrm{peak}} = \max |p(t)|^2$. The temporal duration of the pulse is now defined as:

$$T = \frac{1}{P_{\mathrm{peak}}} \int_0^a |p(t)|^2\, dt. \tag{5.13}$$

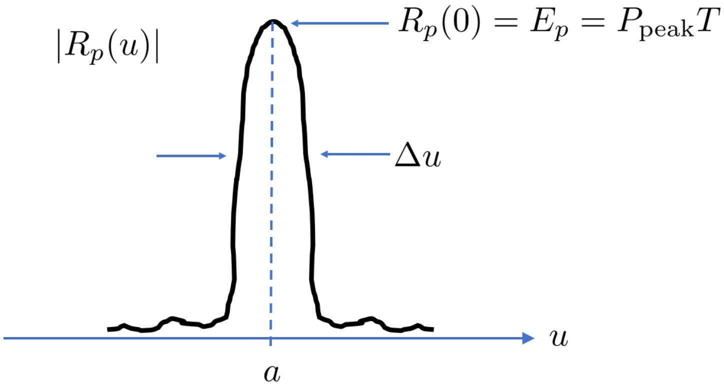

Figure 5.3: Schematic of the autocorrelation peak.

With this definition, the relationship between (peak) power and pulse energy is simply $E_p = P_{\text{peak}}T$. From this it is clear the first lesson in radar theory: systems are usually limited by (peak or average) power, so that in order to increase the SNR for given P_{peak} and N_0 one must increase the temporal extent of the probe pulses.

The pulse bandwidth, in turn, can be defined in several ways, such as 3 dB decay in power, equivalent bandwidth, or bandwidth between nulls in the energy spectral density. There's a nice exposition of all these bandwidth definitions in the book by Soliman and Srinath [20]. All of them differ by a factor of the order of unity that depends on the type of pulse model under consideration. A particularly suitable definition of bandwidth, for the present purposes, is the following effective bandwidth:

$$B = \frac{\left[\int_{-\infty}^{+\infty} S_e(f)df\right]^2}{\int_{-\infty}^{+\infty} S_e^2(f)df} = \frac{E_p^2}{\int_{-\infty}^{+\infty} S_e^2(f)df}.$$

The reason for this choice will be clear soon.

Though the maximum value of the SNR_a (Eq. 5.12) at $u = a$ does not depend on the pulse form $p(t)$, only on its energy, the form of the autocorrelation does depend on it. In Fig. 5.3 there is a schematic image of the situation.

Of particular relevance is the width Δu of the autocorrelation peak, as this value determines the resolution of the radar system. Using the same type of definition as in Eq. 5.13 we have:

$$\Delta u = \frac{1}{R_p(0)^2} \int_{-\infty}^{+\infty} |R_p(u)|^2 du. \tag{5.14}$$

Using the Parseval theorem, this can be alternatively expressed as:

$$\Delta u = \frac{1}{E_p^2} \int_{-\infty}^{+\infty} S_e(f)^2 df$$

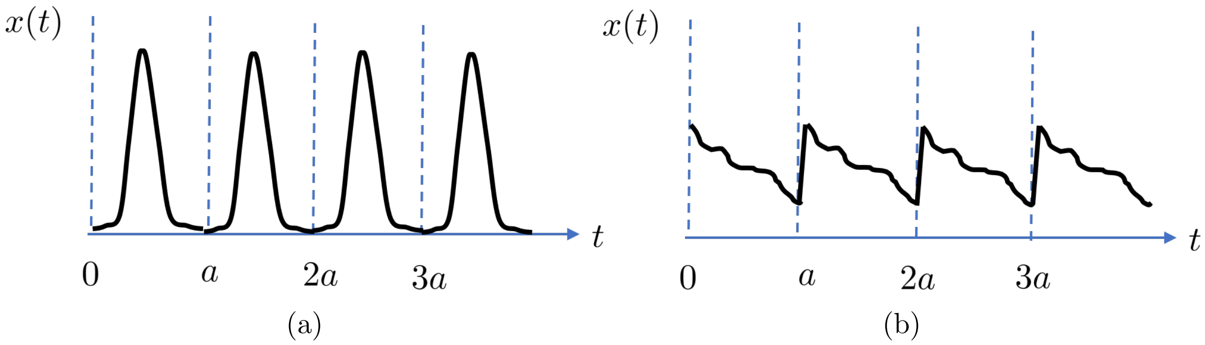

Figure 5.4: Schematic of arbitrary periodic waveforms.

and we find that the autocorrelation width is directly the inverse of the bandwidth,

$$\Delta u = \frac{1}{B}.$$

This is the reason for the aforementioned choice. Now, we define the *compression ratio* as the ratio between the temporal spread of the pulse and the temporal width of the autocorrelation, i.e., the temporal width of the pulse after compression:

$$\frac{T}{\Delta u} = TB.$$

The compression factor represents the natural figure of merit of the pulse compression process and *always* equals the TBP product (with these definitions of T and B). Usually both terms (compression factor and TBP) are used as synonyms. High T implies (for a given peak power), high SNR; and high B implies high resolution.

Let us now consider a more general situation: a matched filter acting over a periodic probe waveform. In fact, this is not the most general situation: one can consider a sequence of, say, M equal pulses and try to detect them with a global matched filter. Levanon discusses these cases. But for our purposes this scenario will be sufficient.

In this case, a periodic signal $x(t)$ is composed of fundamental unit cells, each described by our previous function $p(t)$. Mathematically:

$$x(t) = \sum_{k=-\infty}^{+\infty} p(t - ka).$$

We have assumed that the fundamental period is a. Here we may consider situations where the periodic probe is composed of pulses or of more general waveforms, a fact that is schematically illustrated in Fig. 5.4.

In this case, one can define the pulse width T as before, in terms of the peak power. But now one is also free to refer the pulse width T' to the average power, $\overline{P} = \frac{E_p}{a} =$

$\frac{1}{a}\int_0^a |p(t)|^2 dt$. In this case E_p refers to the energy contained in a single period. This new temporal duration now coincides with a, since

$$T' = \frac{1}{\overline{P}} \int_0^a dt\, |p(t)|^2 = a.$$

Notice that both definitions are interchangeable, since:

$$T' = T\frac{P_{\text{peak}}}{\overline{P}}.$$

In practice, the interesting waveforms are those with a low peak-to-sidelobe ratio, or ideally, $\frac{P_{\text{peak}}}{\overline{P}} \approx 1$, as this can be more easily amplified. From now on we use T' and avoid the use of a. The signal is periodic, and it can be expanded in Fourier series as:

$$x(t) = \sum_n X_n e^{j2\pi n \frac{t}{T'}}. \tag{5.15}$$

The power spectral density is now given by:

$$S_p(f) = \sum_n |X_n|^2 \delta(f - n/T') \equiv \sum_n P_n \delta(f - n/T'),$$

where $P_n = |X_n|^2$ is the power of the n-th spectral line. Correlation detection is implemented by matching the periodic input with $h(t) = p^*(T' - t)$, as before. The output is a periodic autocorrelation:

$$\overline{R}_p(u) = \frac{1}{T'} \int_0^{T'} p(t)^* x(t+u)\, dt. \tag{5.16}$$

The periodic autocorrelation is also a periodic function. Substituting Eq. 5.15 in Eq. 5.16, one readily sees that again the autocorrelation is the Fourier transform of the power spectrum:

$$\overline{R}_p(u) = \int_{-\infty}^{+\infty} S_p(f) e^{j2\pi f u}\, df = \sum_n P_n e^{j2\pi n \frac{t}{T'}}. \tag{5.17}$$

Also, the autocorrelation at zero lag is the total (average) power: $\overline{R}_p(0) = \sum_n P_n = \overline{P}$.

We finally compute the autocorrelation's width, as in the previous example:

$$\Delta u = \frac{1}{\overline{R}_p(0)^2} \int_0^{T'} |\overline{R}_p(u)|^2 du.$$

Inserting the last form of Eq. 5.17 we are led to:

$$\Delta u = T' \frac{\sum_n P_n^2}{\left[\sum_n P_n\right]^2}$$

so that the TBP product or compression ratio is

$$\frac{T'}{\Delta u} = T'B = \frac{\left[\sum_n P_n\right]^2}{\sum_n P_n^2} \equiv N_{\text{eff}},$$

where we have defined the effective number of spectral lines, N_{eff}. This definition is equivalent to considering that the bandwidth is given by $B = N_{\text{eff}}/T'$. The nomenclature of N_{eff} is justified by the fact that, if there is a finite number of spectral lines N, it is necessary that $N_{\text{eff}} \leq N$, the bound being saturated when all the lines carry the same power. This justifies the statement that for a periodic waveform, the TBP or compression ratio equals the number of lines in the optical comb.

C Self-heterodyne method for linewidth measurement

In most lasers, the dominant noise source is spontaneous emission which, as a simple model, may be regarded as emitted photons with the same frequency ν_0 but uniformly distributed random phases ϕ_k in $[0,\ 2\pi)$, a *stationary* process. It can be shown that the variance of the electric field's total phase θ is $\sigma_\theta^2 = \frac{N}{2\bar{n}}$, hence proportional to the number of spontaneous emissions N, $\bar{n}$ being the beam's average number of photons. This follows a process known as *random walk*, of which the mean is zero. Because the number of spontaneous emissions is proportional to time, that is, $N(t) = \frac{n_{sp}}{\tau_c} t$, where n_{sp} is the population inversion factor and τ_c is the cavity lifetime, the phase's variance will then increase linearly with time:

$$\sigma_{\theta(t)}^2 = \frac{n_{sp} h\nu_0}{2{\tau_c}^2 P_{out}} t \equiv \alpha t,$$

$P_{out} = \frac{\bar{n} h\nu_0}{\tau_c}$ being the laser's power output. Since the derivative of phase changes is equivalent to frequency changes, then this corresponds to white frequency noise of which the PSD (Power Spectral Density) is α. Therefore, the PSD of phase noise results f^{-2}:

$$S_\theta\left(f\right) = \frac{\alpha}{\left|j2\pi f\right|^2} = \frac{n_{sp} h\nu_0}{8\pi^2 {\tau_c}^2 P_{out}} \frac{1}{f^2}.$$

From this, and assuming Gaussian differential phase $\Delta\theta = \theta(t+u) - \theta(t)$ fluctuations, it can be proven that the correlation of the electric field is

$$R_E\left(u\right) = A_0^2 e^{j2\pi\nu_0 u - \pi\Delta\nu|u|}$$

and, according to Wiener–Khintchine theorem, the PSD of the total electric field is Lorentzian:

$$S_e\left(\nu\right) = A_0^2 \frac{2/\pi\Delta\nu}{1 + \left[\frac{2(\nu-\nu_0)}{\Delta\nu}\right]^2}.$$

$\Delta\nu$ has been defined as $\Delta\nu = \frac{\alpha}{2\pi}$ and A_0 is the amplitude of the total electric field of which the time fluctuations have been assumed to be negligible. Therefore, the power spectrum of a laser governed by spontaneous emission noise has a Lorentzian shape.

We can then see that $\Delta\nu$ is the FWHM (Full Width at Half Maximum) of the laser's line shape which can be expressed as a function of the resonator mode's FWHM, $\Delta\nu_R = \frac{1}{2\pi\tau_c}$, as

$$\Delta\nu = \frac{\pi n_{sp} h\nu_0 \left(\Delta\nu_R\right)^2}{P_{out}}. \tag{5.18}$$

This is the well-known Schawlow-Townes equation.

In a Mach-Zehnder interferometer —Fig. 2.4—, the measured magnitude is the photocurrent $i_{ph}(t)$. This photocurrent is proportional to the intensity of the field, $i_{ph}(t) = \mathcal{R}i'(t) = \mathcal{R}\left|e'(t)\right|^2$, where $\mathcal{R}$ is the responsivity of the PD (Photodiode) and $e'(t)$ is the electric field at the PD's input, which is the sum of the electric field on the frequency shifted arm $e_{f_0}(t)$ plus the electric field on the delayed arm $e_{\tau_0}(t)$.

If we compute the ensemble average of this photocurrent, we can see that the interference term cancels out only if $\Delta\nu\left|\tau_0\right| \gg 1$, therefore in incoherence regime:

$$\frac{\langle i_{ph}(t)\rangle}{\mathcal{R}} = {A_{f_0}}^2 + {A_{\tau_0}}^2,$$

A_{f_0} and A_{τ_0} being the amplitude of the electric field in each arm.

Assuming that $\langle i_{ph}(t)\rangle$ is DC blocked, let us find the correlation to be

$$\begin{aligned}\langle i_{ph}(t)i_{ph}(t+u)\rangle = 2\mathcal{R}^2 A_{f_0}A_{\tau_0}\langle \cos\left[2\pi f_0 t + \theta(t) - \theta(t-\tau_0)\right] \times \\ \cos\left[2\pi f_0(t+u) + \theta(t+u) - \theta(t+u-\tau_0)\right]\rangle,\end{aligned}$$

where f_0 is the frequency shift, that is, $\nu_{out} = \nu_0 + f_0$. Thus, this photocurrent is statistically nonstationary, and an additional temporal averaging is required. It can be shown that this results in:

$$\overline{\langle i_{ph}(t)i_{ph}(t+u)\rangle} = \mathcal{R}^2 A_{f_0}A_{\tau_0}\cos\left(e^{j2\pi f_0 t}e^{-2\pi\Delta\nu|u|}\right).$$

And, finally, using the Wiener–Khintchine theorem for nonstationary processes, its PSD:

$$S_{i_{ph}}(f) = \frac{1}{2}\mathcal{R}^2 A_{f_0}^2 A_{\tau_0}^2 \frac{1/\pi\Delta\nu}{1+\left[\frac{f-f_0}{\Delta\nu}\right]^2}$$

Therefore, the resulting spectrum is of Lorentzian shape with double FWHM. This means that the HWHM (Half Width at Half Maximum) of the measurements corresponds directly to the FWHM of the laser's linewidth.

D Proof of equation 3.3

The goal is to proof Eq. 3.3, this is

$$2R_e(\tau) = R_s(\tau) + j\mathcal{H}\{R_s(\tau)\}. \tag{5.19}$$

Proof. We begin with the output complex field of the FSL,

$$e(t) = \sum_{n=0}^{N-1} e_n e^{j2\pi n f_s t},$$

and its periodic autocorrelation function (PACF),

$$R_e(\tau) = \langle e^*(t)e(t+\tau)\rangle = \int_0^{1/f_s} e^*(t)e(t+\tau)dt.$$

Performing this computation,

$$\begin{aligned} R_e(\tau) &= \sum_{k=0}^{N-1}\sum_{p=0}^{N-1}\int_0^{1/f_s} e_k^* e_p e^{-j2\pi k f_s t} e^{j2\pi p f_s (t+\tau)} dt \\ &= \sum_{k=0}^{N-1}\sum_{p=0}^{N-1} e^{j2\pi p f_s \tau}\int_0^{1/f_s} e_k^* e_p e^{-j2\pi (k-p) f_s t} dt \\ &= \frac{1}{f_s}\sum_{k=0}^{N-1} |e_k|^2 e^{j2\pi k f_s \tau} \end{aligned}$$

where, in the last part of the equation, it has been used the fact that $R_e(\tau) = 0$ for $k \neq p$. This is the well-known Wiener–Khintchine theorem.

Now, we define

$$s(t) = \mathrm{Re}\{e(t)\} = \sum_{n=0}^{N-1} |e_n| \cos(2\pi n f_s t + \phi_n),$$

with ϕ_n the phase of e_n, and compute its PACF:

$$\begin{aligned} R_s(\tau) &= \int_0^{1/f_s} s(t)s(t+\tau)dt \\ &= \sum_{k=0}^{N-1}\sum_{p=0}^{N-1}\int_0^{1/f_s} |e_k|\,|e_p| \cos(2\pi k f_s t + \phi_k)\cos(2\pi p f_s (t+\tau) + \phi_p) dt \end{aligned},$$

using the same procedure as before,

$$R_s(\tau) = \frac{1}{2f_s}\sum_{k=0}^{N-1} |e_k|^2 \cos(2\pi k f_s \tau).$$

It is easy to see, now, that

$$R_s(\tau) = \frac{1}{2}\mathrm{Re}\left\{R_e(\tau)\right\},$$

therefore, if we compute $R_s(\tau) + j\mathcal{H}\{R_s(\tau)\}$, where $\mathcal{H}\{\cdot\}$ denotes the Hilbert transform, we get

$$\begin{aligned}
R_s(\tau) + j\mathcal{H}\{R_s(\tau)\} &= \frac{1}{2f_s}\sum_{k=0}^{N-1}|e_k|^2\cos\left(2\pi k f_s \tau\right) + j\frac{1}{2f_s}\sum_{k=0}^{N-1}|e_k|^2\sin\left(2\pi k f_s \tau\right) \\
&= \frac{1}{2f_s}\sum_{k=0}^{N-1}|e_k|^2 e^{j2\pi k f_s \tau} \\
&= \frac{1}{2}R_e(\tau).
\end{aligned}$$

□

References

[1] H. Guillet de Chatellus, L. R. Cortés, C. Schnébelin, et al., "Reconfigurable photonic generation of broadband chirped waveforms using a single CW laser and low-frequency electronics", Nat. Commun. 9, 2438 (2018).

[2] C. Schnébelin, J. Azaña, and H. Guillet de Chatellus, "Programmable broadband optical field spectral shaping with megahertz resolution using a simple frequency shifting loop", Nat. Commun. 10, 4654 (2019).

[3] V. Durán, H. Guillet de Chatellus, C. Schnébelin, K. Nithyanandan, L. Djevarhidjian, J. Clement, and C. R. Fernández-Pousa, "Optical frequency combs generated by acousto-optic frequency-shifting loops", IEEE Photon. Technol. Lett. 31, no. 23, 1878-1881 (2019).

[4] H. Yang, M. Brunel, M. Vallet, H. Zhang, and C. Zhao, "Analysis of frequency-shifting loops in integer and fractional Talbot conditions: electro-optic versus acousto-optic modulation", J. Opt. Soc. Am. B 37, 3162-3169 (2020).

[5] V. Durán, L. Djevarhidjian, and H. Guillet de Chatellus, "Bidirectional frequency-shifting loop for dual-comb spectroscopy", Opt. Lett. 44, 3789-3792 (2019).

[6] I. Coddington, N. Newbury, and W. Swann, "Dual-comb spectroscopy", Optica 3, 414-426 (2016).

[7] V. Billault, V. Durán, C. R. Fernández-Pousa, V. Crozatier, D. Dolfi, and H. Guillet de Chatellus, "All-optical coherent pulse compression for dynamic laser ranging using an acousto-optic dual comb", Opt. Express 29, 21369-21385 (2021).

[8] C. R. Fernández-Pousa, "On the structure of quadratic Gauss sums in the Talbot effect", J. Opt. Soc. Am. A 34, 732-742 (2017).

[9] J. Clement, H. Guillet de Chatellus, and C. R. Fernández-Pousa, "Far-field Talbot waveforms generated by acousto-optic frequency shifting loops", Opt. Express 28, 12977-12997 (2020).

[10] J. Clement, C. Schnébelin, H. Guillet de Chatellus, and C. R. Fernández-Pousa, “Laser ranging using coherent pulse compression with frequency shifting loops”, Opt. Express 27, 12000-12010 (2019).

[11] R. Paschotta, “Linewidth”, RP Photonics Encyclopedia (2020). Retrieved from `https://www.rp-photonics.com/linewidth.html`.

[12] R. Paschotta, “Self-heterodyne Linewidth Measurement”, RP Photonics Encyclopedia (2020). Retrieved from `https://www.rp-photonics.com/self_heterodyne_linewidth_measurement.html`.

[13] G. P. Agrawal. *Fiber-optic communication systems*, (Wiley, 2010).

[14] A. S. Mohammed, A. Pavic, V. Racic, “Improved model for human induced vibrations of high-frequency floors”, Eng. Struct. 168, 950-966 (2018).

[15] B. E. A. Saleh, and M. C. Teich. *Fundamentals of photonics*, (Wiley, 1991).

[16] H. Yang, M. Brunel, H. Zhang, M. Vallet, C. Zhao, and S. Yang, “RF up-conversion and waveform generation using a frequency-shifting amplifying fiber loop, application to Doppler velocimetry”, IEEE Photon. J. 9, 7106609 (2017).

[17] Z. Zhang, Y. Liu, M. Burla, and B. J. Eggleton, “5.6-GHz-bandwidth photonic stepped-frequency radar using MHz-level frequency-shifting modulation”, Conference on Lasers and Electro-Optics, OSA, paper AF3M.5 (2020).

[18] M. V. Berry and S. Klein. “Integer, fractional and fractal Talbot effects”, J. of Mod. Opt. 43, 2139-2164 (1996).

[19] N. Levanon and Eli. Mozeson. *Radar Signals*, (Wiley, 2004).

[20] S. S. Soliman and M. D. Srinath. *Continuous and discrete signals and systems* (Prentice Hall, 1999).